Modeling dark matter halos with self-interacting fermions: A polytropic approach

Fabian Hernandez-Gutierrez* and J. Barranco†

Division de Ciencias e Ingenierías, Universidad de Guanajuato, Campus Leon, Postal Code 37150, León, Guanajuato, México

(Received 4 December 2025; accepted 7 July 2026; published 4 August 2026)

In this work we study the possibility of modeling the dark matter content in galaxies as a core-halo model consisting of self-gravitating, self-interacting fermions by means of an effective polytropic equation of state. For the core of the halo, the dark matter fermions are degenerate, while for the halo we have considered two possibilities: the fermions have thermalized as a perfect fluid, or they will follow a standard cold dark matter Navarro-Frenk-White profile. The core density profile is obtained by solving the Tolman-Oppenheimer-Volkoff equations, and their properties are determined by the fermion mass, the central density, and the interaction strength. The mass of the fermion and the strength of the fermion self-interaction are fixed by doing a χ^2 analysis to fit the rotational curves of low surface brightness galaxies. It was found that the fermion mass should be in the range $155.10\ \mathrm{eV} < m_f < 313.26\ \mathrm{eV}$ and the interparticle strength in the range $1465.31 < y < 6002.04$ at 68 C.L. in order to reproduce the rotational curves adequately, in the case when the halo is modeled as a thermalized ideal gas. Similar values are obtained if the halo is modeled following a Navarro-Frenk-White case, namely $42.31\ \mathrm{eV} < m_f < 49.23\ \mathrm{eV}$ and $71.43 < y < 132.65$. Once we fixed the values of the mass of the fermion m_f and the interaction strength y, we tested the core-halo model with data from the Milky Way, local dwarf spheroidal galaxies, and the SPARC database. We have found good agreement between the data and the core-halo models, varying only one free parameter: the central density. Thus a single fermion can fit hundreds of galaxies. Nevertheless, the dark matter halo surface density relation or the halo total mass and radius depend strongly on the model for the halo.

DOI: 10.1103/mxch-8971

I. INTRODUCTION

For most cosmological data the paradigm of lambda cold dark matter (ΛCDM) is suitable and reproduces the observations well enough [1]. The area in which this model has inconsistencies is the galactic scales where the predicted and universal Navarro-Frenk-White (NFW) dark matter profile [2] and observations do not agree. Some of the well-documented problems with ΛCDM at small scales are: the cusp/core problem [3], the missing satellite problem [4], and the too-big-to-fail problem [5]. Lesser known problems include: the satellite plane problem [6], the discrepancy of the baryonic Tully-Fisher relation, inferred from simulations compared to observations [7], and the observed survival of a globular cluster for a Hubble time that is not consistent if galactic halos are cusped, as CDM predicts [8]. Some works that tackle those issues at galactic scale have proposed adding baryonic interaction to the CDM model to deal with them [9–13] but there is no general consensus that baryons will solve all those problems.

CDM is effectively modeled as a perfect fluid with an equation of state (EoS) $p \simeq 0$. In the simplicity of this description lies the difficulty of extracting the properties of the particle associated with dark matter. Furthermore, it is possible that the small scale problems of CDM relies on this pressureless hypothesis. Motivated by today's age of precision cosmology [14] and the necessity to find a solution to the galactic scale problems of ΛCDM, it is time to move beyond the pressureless CDM paradigm. Early attempts to test an equation of state for dark matter at cosmological scales have been done in [15–19]. Those works have constrained a barotropic EOS for DM $p = \omega\rho$ with $-4 \times 10^{-5} < \omega < 1.453 \times 10^{-3}$ [19]. Stronger constraints are obtained at the galactic level [20–23] by fitting the rotational velocities in spiral galaxies. It was found that an effective pressure within the limits obtained by cosmological

*Contact author: f.hernandezgutierrez@ugto.mx
†Contact author: jbarranc@fisica.ugto.mx

studies can be sufficient to explain the rotational curve data and the cores of galaxies.

Another possibility considers that the intrinsic nature of the dark matter particle could solve some of the problems. By the "nature of dark matter," we refer to the essential and irreplaceable properties of DM particles: its mass, spin, and interactions with other particles or itself; information still unknown for dark matter. These attributes influence the way galactic-scale structures are formed. It is of special interest the spin of the particle as it alters the their statistical properties and can lead to different halo shapes and mass distributions. The two main options studied in relation with the spin of dark matter are the fermionic spin $1/2$ particles, like the WIMP and sterile neutrinos, that obey Fermi-Dirac statistics and spin-0 candidates that follow Bose-Einstein statistics, like axions and fuzzy dark matter.

These two possibilities converge when it is realized that both, ultralight fermions and bosons have an intrinsic pressure. Theories like fuzzy cold dark try to solve problems in the CDM paradigm, considering the quantum pressure generated by the Heisenberg uncertainty principle [24]. For candidates with spin $1/2$ the pressure sustaining the galaxy from collapse would come from both the Heisenberg uncertainty principle and the Pauli exclusion principle [25,26], stabilizing it gravitationally due to fermionic quantum degeneration pressure and producing core profiles [27,28]. It has been shown that a Fermi degenerate region must exist in "a physically relevant region" [27], making the self gravitating system a natural quantum macroscopic object, which would make it necessary to consider quantum mechanical calculations to compute galaxy structures at kpc scales and below [29], and turning the classical N-body simulations not appropriate below a certain $r_{\min}$, where quantum mechanical effects are essential, which could explain the issues of N-body simulations at galactic scales.

Fermionic dark matter and self gravitating objects made of fermions have been studied to different degrees of complexity, including transition phases and isothermal envelope [30,31]. Of special notice is the model of Ruffini-Arguelles-Rueda in which halos are constructed by a maximum entropy principle and it has been tested with different observations [32].

The simplest model of a fermionic dark matter model is a degenerate gas of fermions that only interacts with the standard model particles gravitationally. This gas will be degenerate as long as conditions for the degeneracy to apply exist. Outside this region the system would then dilute to the classical isothermal equation of state [33], leading to what is commonly known as a "core-halo" system.

In this work, by simultaneously analyzing the rotational curve of low surface galaxies, we found that it is not possible to model all the galaxies with a single species of fermion if it lacks self-interaction. It is found that each galaxy needs a different value of the mass of the fermion. In the context of dark matter with pressure, it is common to invoke self-interaction between the dark matter particles [34–38]. Self-interaction can mitigate the small scale problems of CDM by producing less dense cores due to elastic scattering. When self-interaction in the model is considered, collisional relaxation can lead to a thermodynamic equilibrium, resulting in a core profile with a polytropic shape [39]. The self-interaction would lead to an isothermal envelope [33].

In general, it is difficult to combine microscopic phenomena with macroscopic objects like the dark matter halos. The mechanism generally used in the literature to include self-interaction and the model of dark matter halos consists in computing the radius where collision of dark matter particles can occur within a Hubble time. From that point inward the halo is considered as a gas with barotropic equation of state.

In the case of dark matter with self-interaction [40], it was found that it is possible to reproduce multiple rotation curves considering a fixed σ/m but that does not explain the nature of the particle. Other possibilities consider modification to the Boltzmann equation in N-body simulations, although the size of the particles in the N body are macroscopic objects with masses of the order of $10^5 M_\odot$.

In this work, we aim to test if self-interacting fermions can form dark matter halos with a core that can adequately reproduce the rotation curves of different galaxies with specific values of mass and self-interaction parameter. The self-interacting fermions are described with a well-motivated equation of state, which will be described in Sec. II. As our focus is on the equation of state, our approach to include self-interaction differs from previous analysis, while still explaining a large number of observables. We will examine a core-halo model in which the core consists of a degenerate gas of fermions and the halo is a perfect fluid with an equation of state $p = \omega\rho$, to test this core-halo model we will also compare it with a case where the core is composed of the same degenerate fermion and the halo is the standard NFW halo. In this model, the fermions interact only gravitationally with the standard model and may also exhibit self-interaction.

The velocity profile is obtained by solving the Tolman-Oppenheimer-Volkoff system that models the degenerate core of the object, and computing the mass profile for each type of halo. This is presented in Sec. III. Taking this system, we fit the rotational velocities of some low-surface brightness (LSB) galaxies and extract the best fit for the mass of the fermion and the self-interaction strength constant. The details of the fit are described in Sec. IV. Next, we show that with the values for m_f and y obtained with the LSB data, it is possible to fit the rotational velocity of the Milky Way. Furthermore, with the same values, we show that the 175 galaxies reported in the SPARC catalog can be fitted by only varying the central density of the dark matter halo. Thus, we conclude that the diversity of galaxies can be well explained by a single fermion with mass $m_f \simeq 45$ eV or $m_f \simeq 300$ eV and a strong self-interacting coupling constant $y \simeq 96$ or $y \simeq 5 \times 10^3$, depending on the halo type.

In the present article we have only considered observations at galactic scales. We will leave the study of dark matter fermions with self-interaction at cosmological scales, via an effective polytropic equation of state, for a future work. Some conclusions and a discussion of the possible signature in the morphology of galaxies for this dark matter particle are drawn in Sec. IX.

II. EQUATION OF STATE FOR DEGENERATE FERMIONS WITH SELF-INTERACTION

In the degenerate limit there are explicit equations that describe the energy density ρ and pressure p, which depend on z, the dimensionless Fermi momentum [41]. For the interaction between fermions, relativistic mean field [42] approach has been been applied to construct the EoS for neutron stars and supernovae [43] or neutralino stars [44]. In our case, following [45] and [46], we effectively introduce a contact term to represent the interparticle interaction between dark matter fermions [46]. The Langrangian for this interaction is

$$\mathcal{L}_{\text{int}} = g\bar{\chi}\gamma_\mu\chi\mathbf{V}^\mu, \tag{1}$$

where the interaction strength is given by $y = gm_f/m_I$ [45], where m_I is the energy scale of the interaction, m_f is the fermion mass, and g is the coupling constant,

$$\rho = \frac{m_f^4}{8\pi^2}[(2z^3+z)(1+z^2)^{1/2} - \sinh^{-1}(z)] + \left(\frac{m_f^2}{3\pi^2}\right)^2 y^2 z^6, \tag{2}$$

$$p = \frac{m_f^4}{24\pi^2}[(2z^3-3z)(1+z^2)^{1/2} + 3\sinh^{-1}(z)] + \left(\frac{m_f^2}{3\pi^2}\right)^2 y^2 z^6. \tag{3}$$

As long as the temperature is below the temperature of degeneracy [47]

$$T < T_{\text{deg}} = \frac{\hbar^2}{2m_f K_B}\left(\frac{3\pi^2\rho(r)}{m_f}\right)^{2/3}, \tag{4}$$

we can take the nonrelativistic limit where $z \ll 1$, that is when the mass of the fermion is much greater than the fermi momentum $m_f \gg k_F$, and find that the equation of state for a free gas of fermions in the nonrelativistic case is

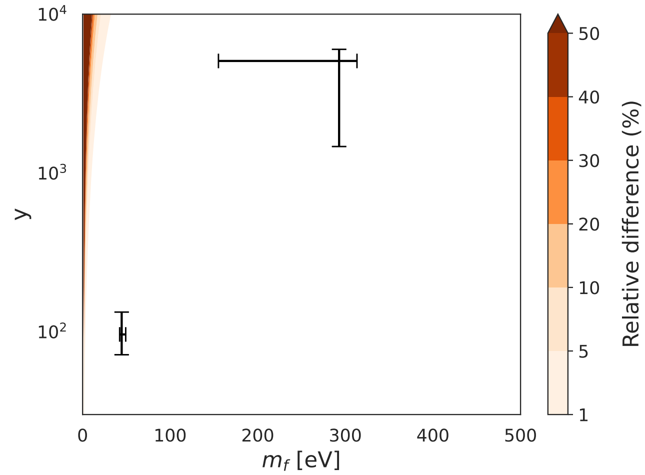

FIG. 1. Relative difference (in %) between the equation of state and its approximation as a function of fermion mass m_f and interaction strength y. The color map shows the contour levels of the relative difference. The black error bars indicate the combined best-fit values (with 1σ uncertainties) obtained from fits to six LSB galaxies, for the NFW halo (bottom) and the perfect-fluid halo (top). The green rectangles correspond to the 1σ confidence regions of the individual galaxy fits.

$$p = \frac{(3\pi^2)^{2/3}}{5}\frac{\rho^{5/3}}{m_f^{8/3}} + \frac{y^2\rho^2}{m_f^4}. \tag{5}$$

To corroborate the validity of this approximation we compared the polytropic equation of state with the full expressions for density and pressure given by Eqs. (2)–(3). As shown in Fig. 1, the polytropic equation reproduces the exact equations to high accuracy, with the results presented in subsequent sections lying within a relative difference of less than 1% across the explored parameter space. This supports the use of the polytropic form for practical purposes in the analysis.

III. SELF-GRAVITATING ULTRALIGHT FERMIONS AS DARK MATTER HALOS

We will model the dark matter content in galaxies as a core consisting of self-gravitating, self-interacting degenerate fermions with an effective equation of state given by Eq. (5). We will consider the system to be spherically symmetric and static. The density profile of the core is found by solving the Tolman-Oppenheimer-Volkoff (TOV) equations. Dark matter cores and halos have low compactness, that is, the system mass is small compared to the radius $GM/r \ll 1$ and $p \ll \rho$, which simplifies the TOV system of equations to the Newtonian TOV equations given by

$$\frac{dp}{dr} = -\frac{GM\rho}{r^2}, \qquad \frac{dM}{dr} = 4\pi r^2\rho. \tag{6}$$

In the case of our equation of state (5) the TOV system can be expressed as

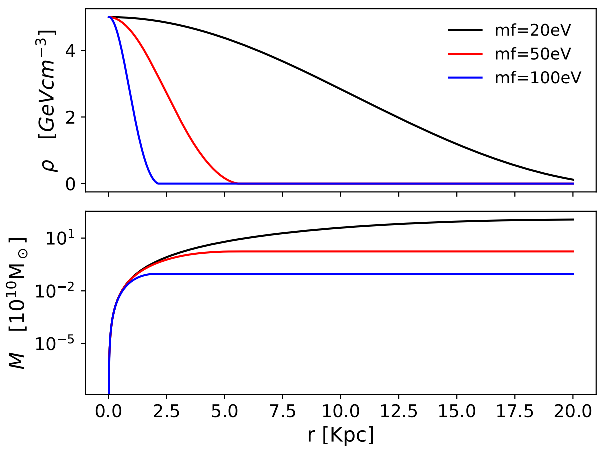

FIG. 2. Density and mass profiles of the self-gravitating system composed of self-interacting degenerate fermions. The left panel shows the changes produced by different values of the fermion mass, with fixed values of $y = 100$, $\rho_0 = 30\ \mathrm{GeV/cm^3}$. The right panel shows the influence of the self-interaction parameter y, with $m_f = 40$ eV, $\rho_0 = 5\ \mathrm{GeV/cm^3}$.

$$\frac{d\rho}{dr} = -\left(\frac{3}{\pi^4}\right)^{1/3} \frac{GM}{r^2} m_f^{8/3} \rho^{1/3} \left[1 + 2y^2\left(\frac{3\rho}{\pi^4 m_f^4}\right)^{1/3}\right]^{-1}, \quad (7)$$

$$\frac{dM}{dr} = 4\pi r^2 \rho. \quad (8)$$

This TOV system is solved numerically, with boundary conditions $M(r = 0) = 0$ and $\rho(r = 0) = \rho_0$, where ρ_0 is the central density of the self-gravitating object and it is a free parameter.

The system's free parameters affect both the size and total mass of the halo. Specifically, lighter fermion masses lead to larger objects, while heavier masses result in smaller ones. Additionally, as the self-interaction parameter increases, the total mass of the system also rises. In Fig. 2, some numerical solutions to the TOV system [Eqs. (7) and (8)] for different elections on the free parameters m_f and y are presented. Left panel of Fig. 2 illustrates the effect of the mass of the fermion for fixed values of $\rho_0 = 5\ \mathrm{GeV/cm^3}$ and $y = 100$. On the other hand, the right panel shows the changes in the mass and density profiles as a function of the self-interaction strength constant y for fixed values of $m_f = 40$ eV and $\rho_0 = 5\ \mathrm{GeV/cm^3}$. Observe that the galactic scale of the self-gravitating object is mainly determined by the ultra light value of m_f.

This description is valid as long as the temperature of the system sits below the degeneracy temperature. The temperature of the system can be determined at any point using the virial theorem

$$T(r) = \frac{2}{7}\frac{GMm_f}{K_b r}, \quad (9)$$

where M is the enclosed mass of the compact object, and r the radial distance where the temperature is

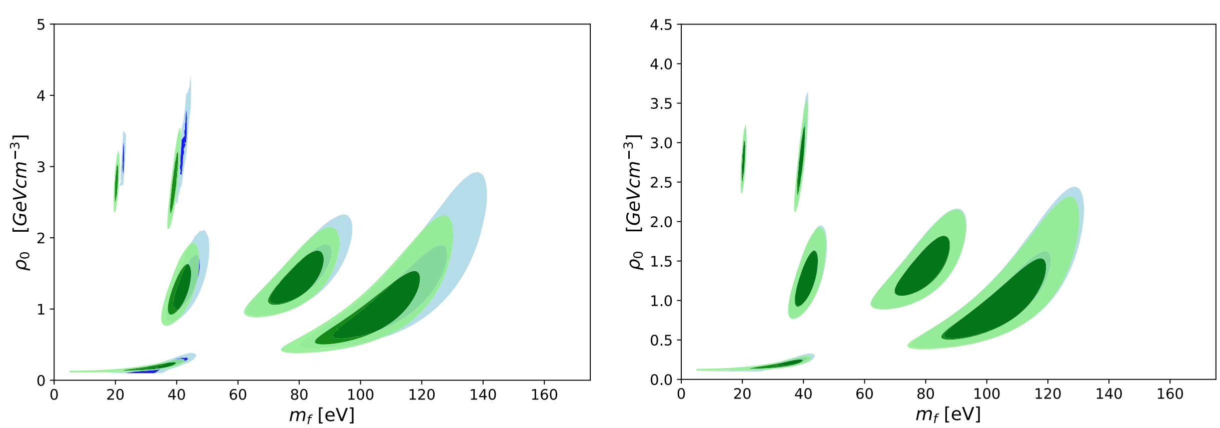

FIG. 3. Contours of the masses of the fermion and central densities allowed by the fit to the rotational curves of the six LSB galaxies studied, in the case of no self-interaction. The darker and lighter regions correspond to the 68% and 95% confidence levels, respectively. The fully degenerate model is shown in green, while the semidegenerate fermion with a NFW halo (left panel) and with a perfect-fluid halo (right panel) are shown in blue.

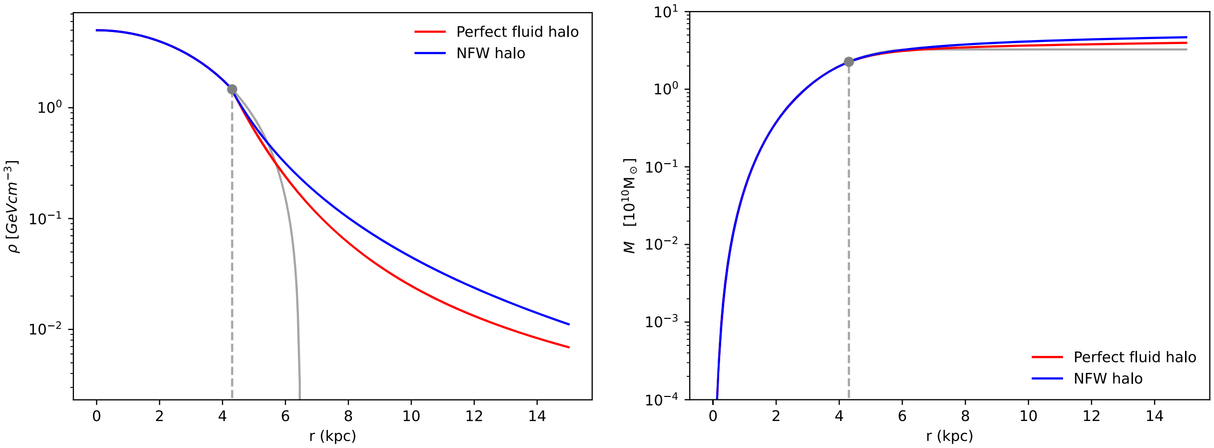

FIG. 4. Density and mass profiles for the core-halo model with the transition point from a degenerate to a nondegenerate system. $\rho_0 = 5\ \mathrm{GeV/cm^3}$, $m_f = 50$ eV, $y = 100$.

computed. Note that the factor $\frac{2}{7}$ comes from the fact that for a polytrope [25]

$$E_{\mathrm{grav}} = -\frac{3}{5-n}\frac{GM^2}{r}, \tag{10}$$

and for a degenerate fermion $n = 3/2$.

If the temperature of the core becomes high enough, according to the virial theorem, the conditions for a fully degenerate gas of fermions are not existent and it will transition into a halo, of which we have chosen two different options: a perfect fluid or a NFW type halo, as shown visually in Fig. 4.

If the gas thermalized, then it would lead to the equation of state of a nonrelativistic classical gas at statistical equilibrium: the classical isothermal equation of state $p = \omega\rho$.

We require hydrostatic equilibrium, and for that to be the case necessitates that $p_{core}(r_*) = p_{halo}((r_*)$, where r_* is the point where the gas stops being degenerate. This means that ω is related to r_* and the model parameters with the equation

$$\omega = \frac{(3\pi^2)^{2/3}}{5}\frac{\rho_*^{2/3}}{m_f^{8/3}} + \frac{y^2\rho_*}{m_f^4}. \tag{11}$$

After the system stops being degenerate the density profile will be obtained by numerical integration. Starting from r_*, the equation for the density of the TOV has the form of

$$\frac{d\rho}{dr} = -\frac{1}{\omega}\frac{GM\rho}{r^2}. \tag{12}$$

The other possibility to model the core halo is the following: we have the same degenerate fermion gas as a core, but as a halo it will have the empirically obtained, and standard, density profile of the ΛCDM model: the NFW profile. The NFW density profile is defined as follows [2]

$$\rho_{\mathrm{NFW}}(r) = \frac{\rho_s}{\frac{r}{R_s}(1+\frac{r}{R_s})^2}, \tag{13}$$

where ρ_s is the scale density and R_s is the scale radius. The system is in virial and dynamical equilibrium, which produce an effective pressure, but in the case of the NFW profile there is no pressure as $\omega = 0$. To ensure a good transition from the degenerate fermion core to the NFW modeled region, we demand that the density and its radial derivative be continuous in the transition radius r_*. This results in the scale radius R_s and the scale density ρ_s being given by the expressions

$$R_s = -r_\star\left[\frac{r_\star\rho'_\star + 3\rho_\star}{r_\star\rho'_\star + \rho_\star}\right], \qquad \rho_s = -\frac{4(r_\star\rho'_\star\rho_\star^3 + \rho_\star^4)}{(r_\star\rho'_\star + 3\rho_\star)^3}, \tag{14}$$

where ρ_* and ρ'_* are the density and it's derivative in $r_\star$.

Both models for the dark matter core-halo system have only three free parameters: the mass of the fermion m_f, its interparticle interaction y, and the central density of the system ρ_0. These parameters influence the size and mass of the system, creating a variety of different possible structures.

In Figure 4 the density and mass profiles for the core-halo models are shown, illustrating the transition point from a degenerate to a nondegenerate system for a perfect fluid halo (red line) and the NFW halo (blue line), for some representative values for m_f and y. Observe that these are smooth profiles in both cases.

With these two core-halo models, we are able to explore the possibility of the inner region of a DM halo being composed of a degenerate gas of self-interacting fermions, capturing what would be the quantum effects of the central region of the halo.

The option of the NFW halo type provides a reference point for the standard results of CDM, which suffers from the *core-cusp problem*, meanwhile the perfect fluid halo corresponds to the nondegenerate case of a fermionic gas, which is a perfect fluid with equation of state $p = \omega\rho$.

IV. FITTING LOW SURFACE BRIGHTNESS GALAXIES

LSB galaxies are dominated by dark matter, which makes the inclusion of baryonic matter unnecessary and makes them good systems to study dark matter properties in galactic scales [48]. For instance, LSB galaxies have shown that CDM is not an appropriate model to describe them [49]. In our case, the dark matter particle is a fermion with mass m_f and self-interaction strength y that fulfills equation of state Eq. (5).

We chose a subset of six of the LSB galaxies presented in [50], which include galaxies with good or fair quality of data and different morphologies, as presented in Table I. In order to obtain the parameters that best reproduce the rotational velocity curves of the six LSB galaxies selected we do a minimum χ^2 analysis to obtain the best-fit values for the fermion mass m_f, the self-interaction parameter y, and the central density ρ_0,

$$\chi^2(\rho_0, m_f, y) = \sum_i \left(\frac{v^{th}(r, \rho_0, m_f, y) - v_i^{\rm obs}}{\delta v_i^{\rm obs}} \right)^2, \qquad (15)$$

where $v_i^{\rm obs}$ is the observed velocity, $\delta v_i^{\rm obs}$ the error in the measurement of v_i and v^{th} is the theoretical value of the velocity, which is computed at the same position where $v_i^{\rm obs}$ was measured. The theoretical value of the velocity is computed as

$$v^{th}(r, \rho_0.m_f, y) = \sqrt{\frac{GM(r)}{r}}, \qquad (16)$$

where the value of $M(r)$ is the result of our self-gravitating system. If the system is below $T_{\rm deg}$ it is obtained through solving numerically the TOV system, presented in Eqs. (7) and (8), with a Runge-Kutta fourth order method and a step size of $h = 0.05$ kpc, which entails an accustomed accumulated error of $O(h^4)$. If the temperature of the system surpasses the degeneracy threshold value, then we need to compute the corresponding NFW mass profile, or integrate numerically the TOV system, in the case of a perfect fluid halo, with the corresponding equation for the density, presented in Eq. (12). The mass of the system is conformed exclusively by the dark matter halo, due to this being LSB galaxies.

To understand the role of the self-interactions and the influence of the different type of halos, we performed fits for three different cases: a purely degenerate fermion ($y = 0$, without halo), a core-halo system (NFW or perfect fluid, $y = 0$), and a core halo with self-interaction ($y \neq 0$).

TABLE I. Characteristics of the LSB galaxies selected for analysis.

Galaxy	Q[a]	Type[b]	$r_{\rm max}$ (kpc)	$N_{\rm data}$
ESO 0140040	1	Sb	29.2	8
ESO 0840411	1	Pec.	8.9	9
ESO 1200211	2	Sa	3.5	14
ESO 1870510	1	dSB	3.04	11
ESO 2060140	1	Sc	11.65	15
ESO 3020120	1	dS	10.95	11

[a]Hα rotation curve quality: 1 = good; 2 = fair; 3 = poor.
[b]Hubble type from [51,52] or the NASA/IPAC Extragalactic Database (NED).

A. No self-interaction ($y = 0$)

Similar models for the dark matter halo considered degenerate fermions with no self-interaction [26–29,53,54]. In the present work, the same model for the dark matter halo is assumed and a χ^2 analysis for a fully degenerate fermion dark matter halo with no interaction is done, i.e., $\chi^2 = \chi^2(\rho_0, m_f, y = 0)$. The constraints for the mass of the fermion and the central density (since we are fixing $y = 0$) are shown in Fig. 3 in darker (68% CL) and lighter (95% CL) green.

In contrast to the models in [26,28,29,53,54], in our case, we consider two models for the halo. By repeating the same analysis for the LSB galaxies but with the inclusion of the NFW halo or the perfect fluid halo, we obtain new allowed regions for m_f and ρ_0. They are shown in Fig. 3 in darker (68% CL) and lighter (95% CL) blue.

In both cases we may conclude that the mass of the fermion are quite narrow and differ from galaxy to galaxy, needing a different value for the fermion mass to fit each of the LSB galaxies studied. Adding a halo to the degenerate fermion core doesn't improve substantially, but it does broaden the allowed regions of the m_f parameter. Specially for the case where the halo is modeled as a perfect fluid (see left panel of Fig. 3).

B. With self-interaction $y \neq 0$

We arrive at the central point of this work: can self-interaction alleviate the need of different fermions for each galaxy under study? In order to answer this question, we perform a χ^2 analysis with $y \neq 0$, i.e., $\chi^2 = \chi^2(\rho_0, m_f, y \neq 0)$. The results for the projected values allowed for m_f and ρ_0 are shown in Fig. 5. Color code for $y \neq 0$ is: darker red isocurves for 68% CL and lighter red isocurves for 95% CL. For comparison we have included in the same plot as in the previous section for the case with no

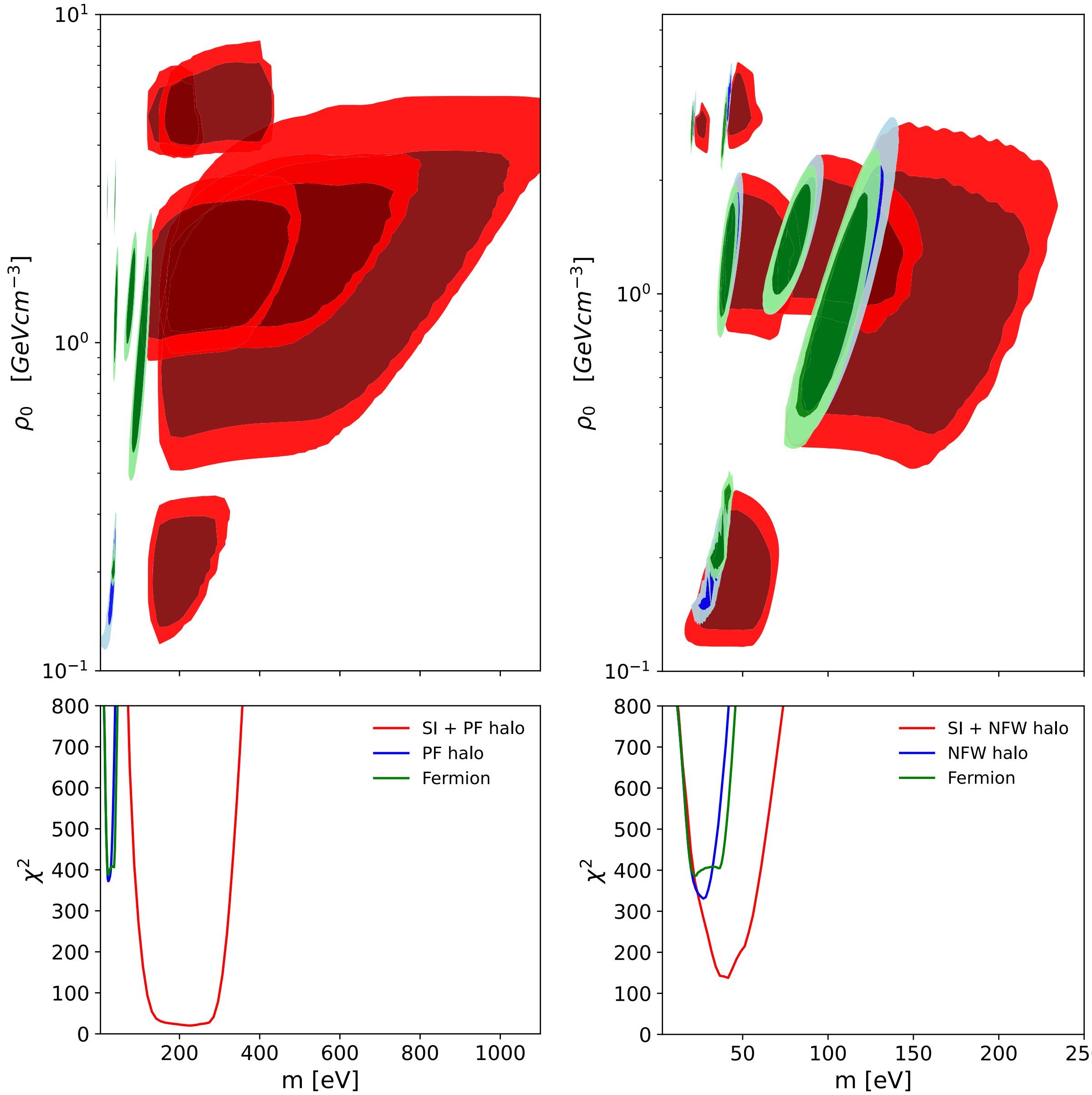

(a) Perfect Fluid halo

(b) NFW halo

FIG. 5. Comparison of fits for the perfect-fluid (a) and NFW (b) halo models. Top panels: contour for the 68% and 95% confidence levels for the three possible cases: a self-interacting fermion with halo (red), a noninteracting fermion with halo (green), and the fully degenerate fermion (blue). Bottom panels: χ^2 as a function of the fermion mass for each of the same models.

self-interaction, $y = 0$. For $y = 0$ isocurves, the color code is the same as in Fig. 3.

It can be seen that the core-halo model broadens the allowed parameter space, and these regions become even larger when self-interactions are included. The Fig. 5 also display the projection of the sum of the χ^2 as a function of the fermion mass, m_f, the parameter that is required to be common to all galaxies. The χ^2 curves indicate that the case with both a halo and self-interactions provides fits that are comparable to, or better than, those obtained with the previous cases.

The fit of the rotational curves was performed by a χ^2 minimization over a three-dimensional parameter grid to obtain the best-fit values for the fermion mass m_f, the self-interaction parameter y, and the central density ρ_0. The grid resolution was $100 \times 100 \times 100$ (10^6 points). The self-interaction parameter was sampled using a log-uniform (geometric) spacing, while the remaining parameters were sampled linearly within their respective ranges.

The best fit points obtained are presented in Table II. They show that χ^2/d.o.f. (degrees of freedom) is smaller than unity for the halo modeled as a ideal gas, while the

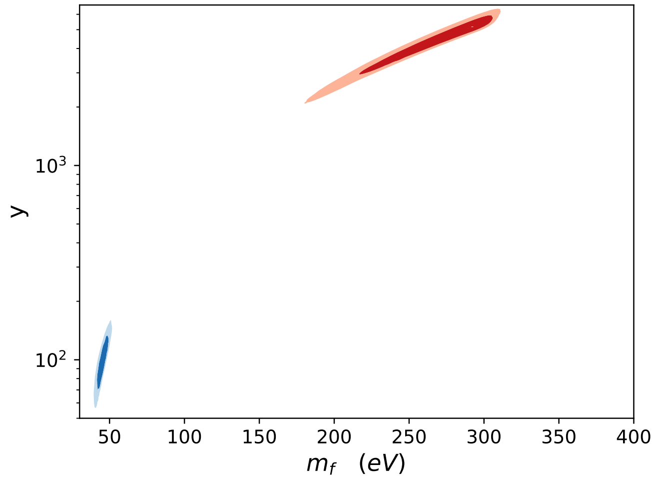

FIG. 6. Masses and interaction parameters allowed to fit the rotational curve data of the different galaxies studied. The contours represent the 68% (darker shade) and 95% (lighter shade) confidence limits. In red we present the contours for the case with a perfect fluid halo, in blue the NFW halo case.

halo modeled with a NFW density profile gives reasonable fits with $\chi^2/\mathrm{d.o.f.} \sim 1$. This results suggest that a reduction on the free parameters is possible. In particular, we are interested in the dark matter particle properties, which for our case are m_f and y. To obtain the information of the two parameters that are of interest, the fermion mass and the self interacting parameter, we did a combined minimum χ^2: $\chi^2_{\mathrm{combined}} = \sum_{i=1}^{n} \chi^2_{p_i}$, where $\chi^2_{p_i}$ is the profiled chi-squared statistic for the ith dataset.

The results of the combined fit minimized in ρ_0 and projected in the (m_f, y) plane are shown in Fig. 6 where we present the contours of the parameters that fit the data with 1σ (68% CL) and 95% confidence levels. Dark and light blue are isocurves for the degenerate core with a NFW halo while the dark and light red correspond to isocurves for the degenerate core with a ideal gas equation of state for the halo. In summary, the fit values of the combined χ^2 are:

(i) For the NFW halo

$$m_f = 44.62^{+4.61}_{-2.31}\ \mathrm{eV}, \qquad y = 95.92^{+36.73}_{-24.49}, \tag{17}$$

(ii) For the perfect fluid halo

$$m_f = (2.93^{+0.2}_{-1.38}) \times 10^2\ \mathrm{eV}, \quad \mathrm{y} = (5.07^{+0.93}_{-3.61}) \times 10^3. \tag{18}$$

There is only one free parameter left in the model: the central density of the system, a value that is case specific for each of the galaxies. We finish this section by fixing m_f and y in the equation of state Eq. (5) and perform a $\chi^2 = \chi^2(\rho_0)$ analysis of our sample rotational data of the six LSB galaxies. These fits gave good results and are presented in Table III for the model with a halo with a barotropic equation of state and Table IV for a halo with a NFW density profile.

In general, even with one free parameter, a self-interacting fermion with a defined mass and self-interaction strength fixed gives reasonable fits. For reference, the predicted rotational curve and a comparison with the data are shown in Fig. 7, where we also have plotted the predicted rotational curve for the best fit values obtained by

TABLE II. Best fit values for a core-halo system with a core of a degenerate fermion with self-interaction and a NFW halo of perfect fluid halo.

	Perfect fluid halo				NFW halo			
Galaxy	$\chi^2/\mathrm{d.o.f.}$	m_f (eV)	y	ρ_0 $(\mathrm{GeV/cm^3})$	$\chi^2/\mathrm{d.o.f.}$	m_f (eV)	y	ρ_0 $(\mathrm{GeV/cm^3})$
ESO0140040	0.982	198.485	3684.031	4.771	3.646	25.882	64.037	2.902
ESO0840411	0.062	196.566	5139.043	0.193	0.099	35.941	52.160	0.192
ESO1200211	0.080	270.707	1239.429	1.160	0.184	108.824	57.794	0.944
ESO1870510	0.045	428.788	4417.470	1.721	0.193	85.294	96.519	1.302
ESO2060140	0.353	463.636	8091.108	5.487	2.257	41.765	28.187	2.944
ESO3020120	0.003	190.909	1893.240	1.605	0.184	44.118	38.344	1.302

TABLE III. Best fit results for a model with a perfect fluid halo and fixed parameters $m_f = 292.86eV$ and $y = 5071.43$.

Galaxy	ρ_0 $(\mathrm{GeV/cm^3})$	$\chi^2/\mathrm{d.o.f.}$
ESO0140040	10.028	3.558
ESO0840411	0.442	1.886
ESO1200211	0.329	0.999
ESO1870510	0.835	1.128
ESO2060140	2.580	2.171
ESO3020120	1.361	0.081

TABLE IV. Best fit results for a model with a NFW and fixed parameters $m_f = 44.62eV$ and $y = 95.92$.

Galaxy	ρ_0 $(\mathrm{GeV/cm^3})$	$\chi^2/\mathrm{d.o.f.}$
ESO0140040	11.140	24.904
ESO0840411	0.249	0.392
ESO1200211	0.268	1.427
ESO1870510	0.715	1.808
ESO2060140	1.983	3.177
ESO3020120	0.976	0.428

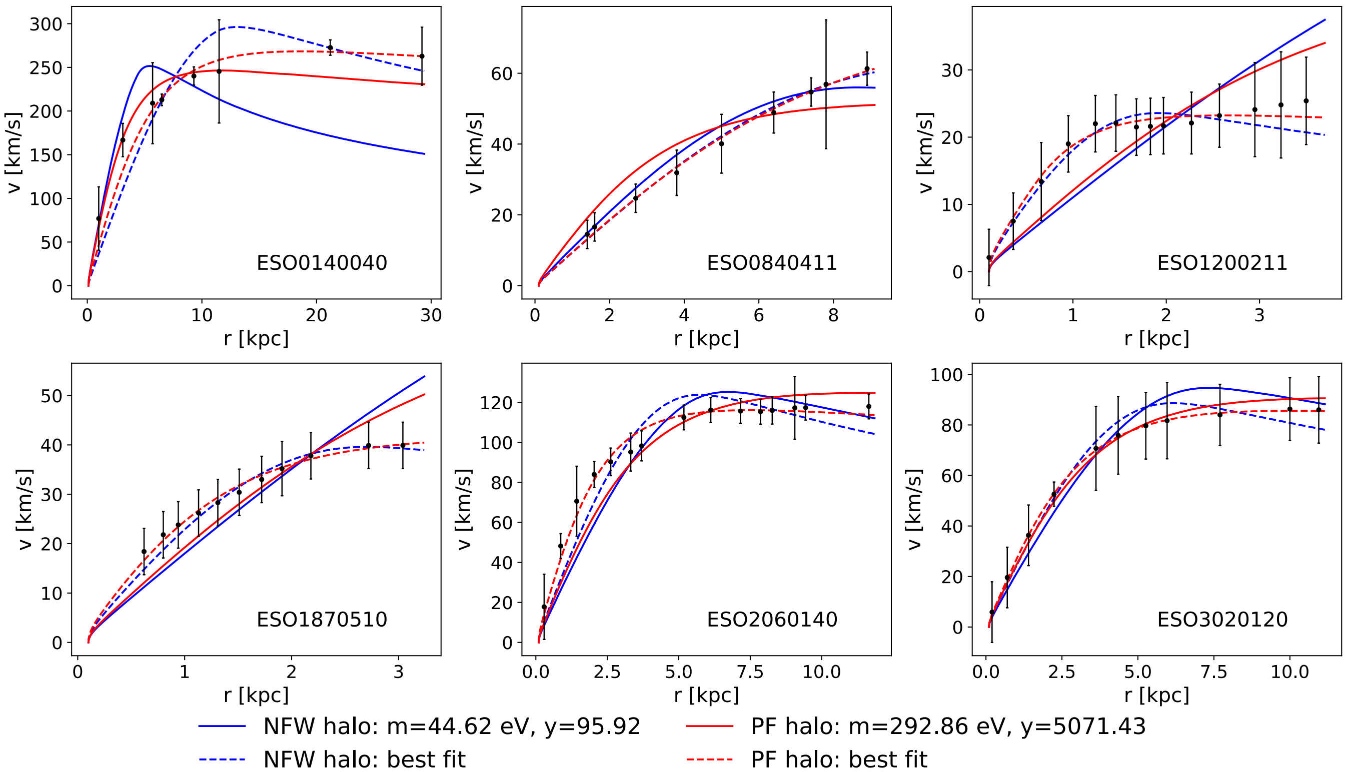

FIG. 7. Rotation curves for the LSB galaxy sample. Solid curves show the best-fit results, shown in Table II; dashed curves show the predicted curves when the fermion mass mf and self-interaction parameter y are fixed. Perfect-fluid halos (red) use $m_f = 292.86$ eV, $y = 5071.43$; NFW halos (blue) use $m_f = 44.62$ eV, $y = 95.92$. The central density values for each of the galaxies and χ^2/d.o.f. are presented in Tables III and IV.

minimization of χ^2 by varying the three parameters as shown in Table II.

V. THE MILKY WAY ROTATIONAL CURVE

Having found values of the fermion mass and interaction parameter that reproduce well enough the rotational curves of the LSB galaxies [see Eqs. (17), (18)], we can use these values to predict the rotational curve of different systems. First, we will test the model with the Milky Way's rotational curve. Measurements of the rotational velocity of the Milky Way are divided in components related to the structure of the galaxy: the central black hole, the inner bulge or core of the galaxy, the main bulge and the disk of the galaxy. In addition to these four elements, we will add a dark matter core halo as we have explained in the previous Section.

The data covers a wide range of radius: from 1 pc to several hundred kpc, without a gap of data points. This was achieved by combining data from the outer disk and analyzing high-resolution longitude-velocity diagrams of the galactic center, observed with the Nobeyama telescope in the carbon monoxide and carbon monosulfide line emissions. There are 67 data points that go from 1.12 pc to 1,600 kpc [55,56].

The disk, inner bulge, and main bulge can be modeled by an exponential sphere model, in which the mass density of the region $\rho_R(r)$ is given by,

$$\rho_R(r) = \rho_R^c \exp(-r/a_R), \tag{19}$$

where ρ_R^c corresponds to the central density of the region R, and a_R to its scale radius. The values of the parameters ρ_R^c and a_R are fixed to the values shown in Table V [55,56].

Integrating Eq. (19) for the mass density we are able to find the mass as a function of the radius M_R

$$M_R(r) = 8\pi a_R^3 \rho_R^c \left(1 - e^{-r/a_R}\left(1 + \frac{r}{a_R} + \frac{1}{2}\left(\frac{r}{a_R}\right)^2\right)\right). \tag{20}$$

The velocity of a test particle subject to the mass $M_R(r)$ will be given by

TABLE V. Values used to fit the different sections of the Milky Way rotational velocity [55,56].

Region (R)	Total mass ($10^{10} M_\odot$)	Scale Radius a_R (kpc)
Inner bulge (IB)	5.0×10^{-3}	3.8×10^{-3}
Main bulge (MB)	8.4×10^{-1}	1.2×10^{-1}
Disk (D)	4.4	1.3

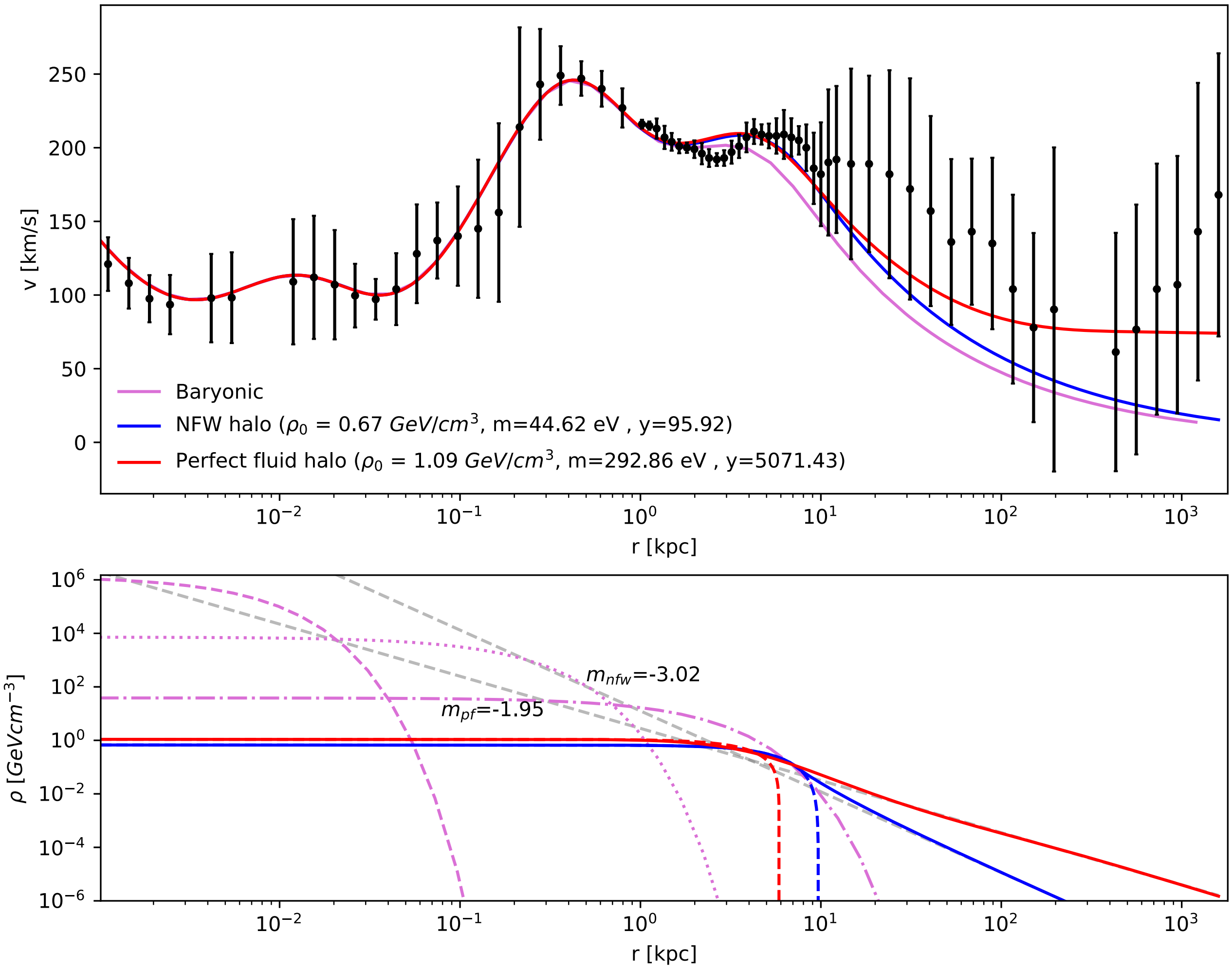

FIG. 8. Milky Way rotational velocity curve obtained for the two core-halo models with fixed values of the fermion mass and the self-interaction parameter given by Eqs. (17) and (18). Plots were done with the best fit for the only free parameter ρ_0. For the NFW-type halo, the fit return a best fit for the central density of $\rho_0 = 0.67\ \mathrm{GeV\,cm^{-3}}$, whereas the perfect-fluid halo requires $\rho_0 = 1.09\ \mathrm{GeV\,cm^{-3}}$. The lower panel shows the corresponding density profiles for the different components of the Milky Way.

$$v_R^2(r) = \frac{GM_R(r)}{r}, \tag{21}$$

with $R = IB, MB, D$. Sagittarius A*, the supermassive black hole located at the center of the Milky Way contributes to the total mass, hence, to the velocity of the stars in the galaxy. This contribution will be modeled as a point mass and given by

$$v_{\mathrm{BH}}^2 = \frac{GM_{\mathrm{BH}}}{r}. \tag{22}$$

The mass of the central black hole has been constrained to $4.1 \pm 0.6 \times 10^6 M_\odot$ [57]. We used the central mass value to calculate the rotational velocity contribution of the Sagittarius A*.

$v_{\mathrm{DM}}(r)$ is computed with Eq. (16) with the mass of the dark matter halo obtained by solving Eqs. (6) for the two models for the halo. The theoretical rotational velocity can be obtained from the expression

$$v^{th}(r) = \sqrt{\sum_{R=IB,MB,D} v_R^2(r) + v_{\mathrm{BH}}^2(r) + v_{\mathrm{DM}}^2(r)}, \tag{23}$$

where IB is the inner bulge, MB is the main bulge, D is the disk, BH corresponds to the black hole, and DM to the dark matter halo. The velocity from each section of the Milky Way is Eq. (21), where the mass of IB, MB, and D is obtained from Eq. (20).

Having fixed the scale radius a_R and central densities of the baryonic components ρ_R^c of the Milky Way with the values reported in Table V, then the baryonic content of the Milky Way is fixed. By fixing the fermion mass m_f and the self interaction parameter y with the central values of Eqs. (17) and (18) for the NFW and perfect fluid halos, the only free parameter in $v^{th(r)}$ to fit the rotational velocity data of the Milky Way is the central density of the core-halo system that model the dark matter halo. The theoretical rotational velocity obtained from computing (23) was compared and fitted to the values reported in [55,56]. The best fit point for the rotational curve of the Milky Way is $\rho_0 = 0.67\ \mathrm{GeV/cm^3}$ with a good fit given by a $\chi^2/\mathrm{d.o.f.} = 0.93$ for the case with a NFW halo. Similarly, we get $\rho_0 = 1.09\ \mathrm{GeV/cm^3}$ with a $\chi^2/\mathrm{d.o.f.} = 0.88$ for the case with a perfect fluid halo. In Fig. 8 we plot the predicted rotational velocity curve for the two cases overlapped with the data reported by [55,56]. The blue line corresponds to the case of a NFW halo while the red line is the case for a perfect fluid with barotropic equation of state. For comparison we have included the case where no dark matter is included in a light purple line. In the bottom panel of Fig. 8 is plotted the density profile, including the baryonic contribution. Baryonic matter dominates the stellar dynamics at radius smaller than one kiloparsec, and dark matter stars dominate only for larger radius. The halo with a barotropic equation of state fits better that the NFW halo. For $r \gg 1$ kpc the halo mass density $\rho(r)$ follows a power law decay. In particular, as expected, the NFW decays as $\rho(r) \sim r^{-3}$ while the perfect fluid halo decays as $\rho(r) \sim r^{-2}$ as can be seen in the lower panel of Fig. 8. This change in the decay of the mass density implies that the total mass of the core-halo system differs. These differences could be important in the determination of the stellar dynamics and thus lead to possible routes towards a better understanding of the structure of the dark matter halos.

VI. MILKY WAY'S DWARF GALAXIES

Now we test both core-halo models with the *classical* Milky Way's dwarf spheroidal galaxies. Those galaxies are low-luminosity, low-surface-brightness, satellite galaxies characterized by a high-quality datasets of the projected velocity dispersion along the line of sight as a function of the projected radius $\sigma_{LOS}(r)$. In these galaxies, rotation is negligible and the stars are in equilibrium against gravity by their random motion. Assuming spherical symmetry, with constant orbital anisotropy β, the observed projection of the velocity dispersion along the line of sight at the projected radius r is given by

$$\sigma^2_{LOS}(r) = \frac{2G}{I(r)} \int_r^\infty \nu(r') M(r') (r')^{2\beta-2} F(\beta, r, r') dr'. \tag{24}$$

Here

$$\nu(r) = \frac{3L}{4\pi r^3_{half}} \frac{1}{(1 + (r/r_{half})^2)^{5/2}}, \tag{25}$$

is the three-dimensional spherically symmetric stellar density with total luminosity L for a Plummer profile. r_{half} measures the radius within 50% of a galaxy's total emitted light (luminosity) is contained. Furthermore, for a Plummer profile for stellar density

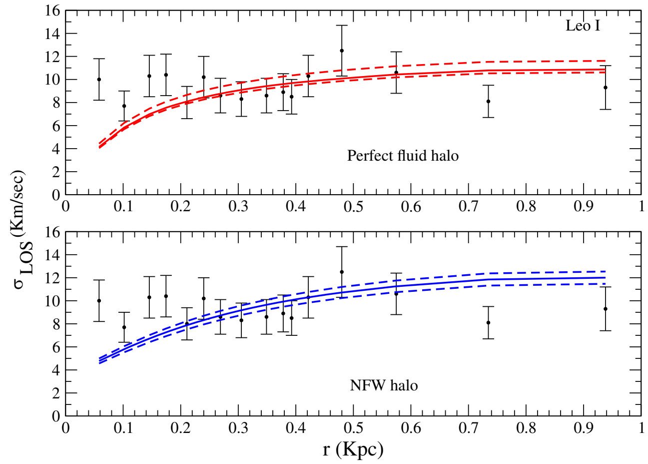

FIG. 9. Fit for σ_{LOS} for the dwarf spheroidal galaxy Leo I data. Upper panel corresponds to the perfect fluid halo, dashed lines are $1-\sigma$ deviation for the best fit parameter as reported in Table VI. Lower panel corresponds to the NFW halo model.

$$I(r) = \frac{L}{\pi r^2_{half}} \frac{1}{(1 + (r/r_{half})^2)^2}. \tag{26}$$

The factor that parametrizes the projection over the line of sight is given by

$$F(\beta, R, r') = \int_R^{r'} \left(1 - \beta \frac{R}{r^2}\right) \frac{r^{-2\beta+1}}{\sqrt{r^2 - R^2}} dr. \tag{27}$$

We compute the theoretical σ_{Los} where the information of the dark matter halo is encoded in the mass $M(r)$ of the halo obtained by solving Eqs. (6) for the two models for the halo. For simplicity we have assumed $\beta = 0$, which means that velocities are isotropic. Relaxing this assumption will just improve the fit. Empirical velocity dispersion profiles for the eight "classical" dwarf-spheroidal galaxies were obtained from [58–61].

We performed a χ^2 analysis by computing the theoretical $\sigma_{LOS}(r)$ by means of Eq. (24) by fixing the mass of the dark matter fermion m_f and the self-interaction strength y for the two core-halo models. The only free parameter is the central density ρ_0. The results are shown in Tables VI

TABLE VI. Best fit results for the dispersion velocities of the Milky Way satellite galaxies for a model with a perfect fluid halo and fixed parameters $m_f = 292.86eV$ and $y = 5071.43$.

Galaxy	ρ_0 $(\mathrm{GeV/cm^3})$	χ^2	$\chi^2/\mathrm{d.o.f.}$
Leo I	0.554	25.352	1.690
Leo II	0.450	24.690	2.469
Draco	0.581	13.279	0.830
Carina	0.450	123.857	4.763
Fornax	0.456	213.908	4.551
Sculptor	0.559	123.513	3.529
Sextants	0.449	103.554	7.397
Ursa Minor	0.613	37.277	2.662

TABLE VII. Best fit results for the dispersion velocities of the Milky Way satellite galaxies for a model with a NFW halo and fixed parameters $m_f = 44.62eV$ and $y = 95.92$.

Galaxy	ρ_0 (GeV/cm^3)	χ^2	χ^2/d.o.f.
Leo I	0.485	30.0627	2.004
Leo II	0.346	24.567	2.457
Draco	0.505	15.511	0.969
Carina	0.247	66.957	2.575
Fornax	0.366	260.274	5.538
Sculptor	0.505	140.991	4.028
Sextants	0.208	50.795	3.628
Ursa Minor	0.545	40.769	2.912

and VII for both the fluid and NFW halo models. As an illustration, in Fig. 9 are shown the best fit for the dwarf spheroidal galaxy Leo I. As before, the model fits the data of a dwarf spheroidal with only one free parameter left: the central density.

VII. FITTING THE SPARC DATABASE

Next, we test the core-halo models with fixed m_f and y with a larger database. For definitiveness, we use the *Spitzer* Photometry and Accurate Rotation Curves (SPARC) database. It contains 175 galaxies that cover a wide spectrum of morphologies, luminosities, and surface brightness [62]. The database include both the data of the rotation curve of the galaxy and the inferred contribution of the baryonic components of the galaxy: the gas, the bulk, and the disk. The theoretical velocity of rotation for a test particle is given by,

$$V_{bar} = \sqrt{|V_{\rm gas}|V_{\rm gas} + \Upsilon_{\rm disk}|V_{\rm disk}|V_{\rm disk} + \Upsilon_{bul}|V_{bul}|V_{bul}} \tag{28}$$

where $\Upsilon_{\rm disk}$ and Υ_{bul} are the stellar mass-to-light ratios of disk and bulge components, respectively [62].

Unlike LSB galaxies where dark matter dominates the dynamics of the rotational curve, the baryonic matter present in the galaxy represents a significant part of what gives the rotational curve its shape. Of special interest is the mass-to-light ratio of the disk and bulge components of the galaxy, as modeling galaxy masses is often affected by uncertainties in the stellar mass-to-light ratio, which influence the relative contributions of the dark matter halo and the stellar disk to the rotational curve [63]. To prevent these uncertainties and focus on the parameters of our model, we fix $\Upsilon_{\rm disk}$ to 0.5 and Υ_{bul} to 0.7, these values have been estimated as acceptable for most galaxies at $\mu_{3.6}$ [64–69].

Taking this into consideration, we fitted the SPARC database with the values that best reproduce the six LSB galaxies analyzed in Sec. IV, i.e., Eqs. (17) and (18). The χ^2 function is computed in this case by computing the theoretical velocity

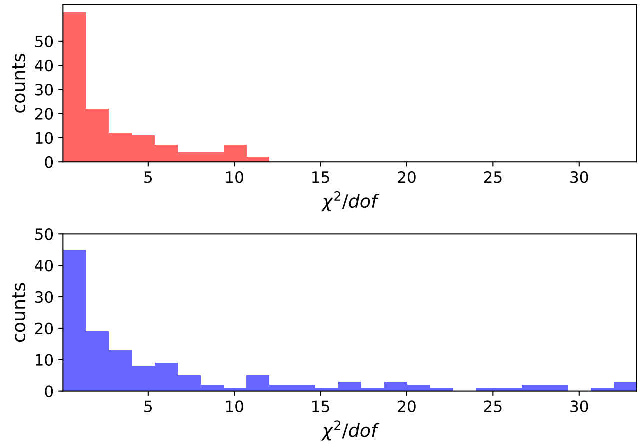

FIG. 10. Distribution of χ^2/d.o.f. values obtained from the fits to the SPARC rotation-curve dataset. The upper panel shows the histogram for the perfect fluid case, while the lower panel displays the NFW halo case. In both cases the histogram is truncated at the 75th percentile in order to highlight the bulk of well-fitted galaxies.

$$v^{th} = \sqrt{V_{bar}^2 + v_{\rm DM}^2(r)}, \tag{29}$$

with $v_{\rm DM}(r)$ computed as in the previous Sec. V.

This procedure gave good results with a median χ^2/d.o.f. of 2.93 for the perfect fluid halo, meanwhile a 5.64 median value for the NFW case (see Fig. 10). The full results are presented in the Table VIII in the Appendix. In this table, the first column refers to the name of the galaxy. The two cases for the halo model are reported: the NFW halo and the perfect fluid halo. For each case we report: the first column is the best fit value for the central density ρ_0 in units of GeV/cm^3 obtained form the fit as explained in Sec. V. The second column shows the minimum value of the χ^2 function and the third column the goodness of the fit expressed with the value of the minimum of the χ^2 function divided by the degree of freedom.

A summary of the goodness of the fit for the SPARC database is represented in the histograms that are shown on the Fig. 10. The full results are presented in Tables IX–XII. If the halo consists of a perfect fluid halo 58 galaxies (33%) fall below χ^2/d.o.f. $= 1$, and 105 (60%) fall below χ^2/d.o.f. $= 5$. On the other hand, in the case of a NFW density profile halo, 35 galaxies have χ^2/d.o.f. lower than unity (20%), and 83 galaxies have χ^2/d.o.f. < 5 (47.43%). Note that the only free parameter is the central density, thus a single fermion with mass of $m_f = 292.86$ eV ($m_f = 44.62$ eV) and interaction strength constant $y = 5.07 \times 10^3$ ($y = 95.92$) can model nearly 200 cores of very different galaxies with a perfect fluid (NFW) halo.

VIII. DISCUSSION

The existence of universal relations between the central density and size of the DM halos of galaxies, their core

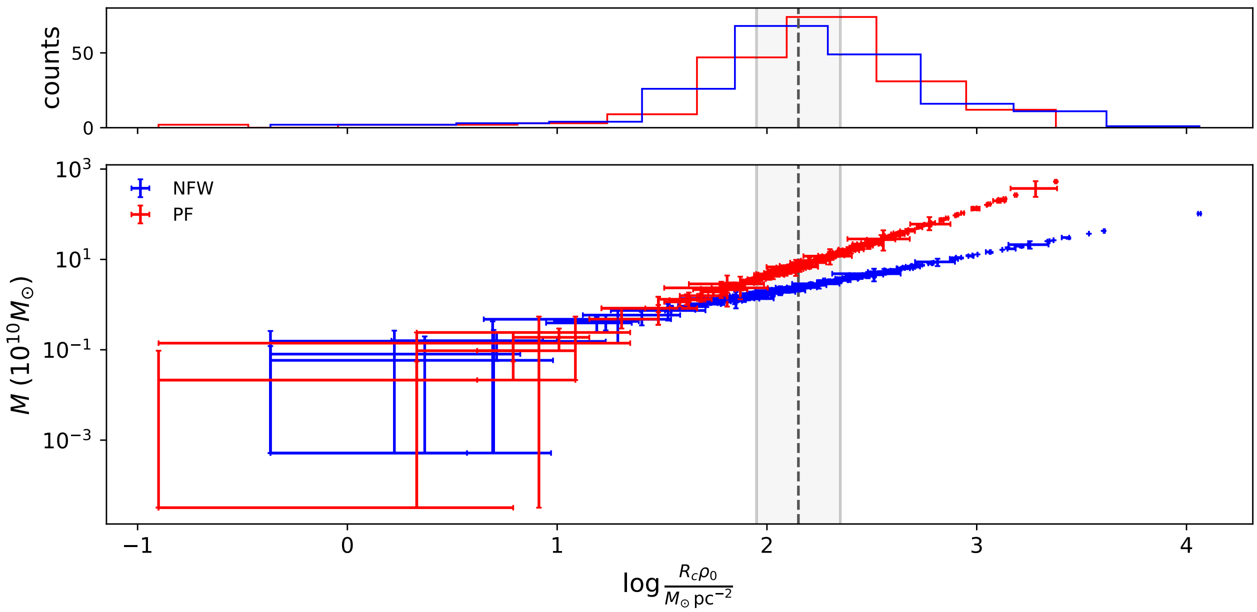

FIG. 11. Total mass as a function of the central surface density $\mu_0 = R_c\rho_0$. The shaded region corresponds to the range of values reported in [70]. In red we present the perfect fluid halo results, and in blue the NFW case. In the upper panel we show the histogram of galaxy counts as a function of μ_0.

radius, or the total mass enclosed at some typical scales, among other relations, may provide relevant information in order to test dark matter candidates. For instance, one scaling relation of interest for dark matter halos is the nearly constant value found in [70,71]. It was found that

$$\log\left(\frac{R_c\rho_0}{M.pc^{-2}}\right) = 2.15 \pm 0.2, \tag{30}$$

where R_c is the core radius and the product $\mu_0 = R_c\rho_0$ is called the central surface density.

Next, we explore if the resulting halos obtained with with our core-halo models, with fixed fermion mass and self-interacting parameters as explained above, will have the same structural relations for μ_0 as Eq. (30).

In our case, we proceed as follows: we compute the core radius R_c as defined by [70], this is where the density of the system is one fourth of the central density, as they assumed that the DM halos follow a Burkert density profile. In the core-halo model we construct here, we adopt the same definition for R_c, although a more convenient definition for our core could be the transition point of the semdegenerate system. Since we have fixed m_f and y with the best fit points, i.e., Eqs. (17) and (18), the only free parameter is ρ_0, thus we compute μ_0 with the best fit point for each galaxy. The results are shown in Fig. 11. Note that of the 182 galaxies analyzed in this work, ~35% fall between the ranges presented in [70,71], for either of the core-halo cases. In the upper panel of Fig. 11, we have plotted a histogram that counts the number of galaxies where μ_0 satisfies Eq. (30). It is interesting that the average coincides with the relation found in [70,71] but with a wider range for μ_0. The lower panel of Fig. 11 shows the total mass M of the core-halo configuration as a function of $\log(\mu_0)$. Unlike the constant values reported, in our model there is a clear exponential relation between μ_0 and M. We find for the perfect fluid halo

$$M = 2.28 \times 10^{-6}\mu_0^{3.54}, \tag{31}$$

and for the NFW halo,

$$M = 1.26 \times 10^{-4}\mu_0^{2.19}. \tag{32}$$

Future analysis or measurements of μ_0 can then be compared with this functional dependence of the core-halo mass.

Our analysis relies on the hypothesis that a self-interacting fermion can be described as a perfect fluid with EOS given by Eq. (5) and two models for the halo. The free parameters of the EOS are fixed by the LSB data. The values found for m_f and y are in a region that agrees with the full expressions for the pressure p and mass density given by Eqs. (3) and (2) as can be seen in Fig. 1.

The structural properties of the core-halo are then a consequence of hydrostatic equilibrium. This analysis does not differ from that of polytropic self-gravitating objects: given a specific EOS, there is a unique family of self-gravitating objects. The characteristic size of the system is defined by the virial radius $r_{\rm vir}$, which is the point where $\rho(r_{\rm vir}) = 200\rho_c$, where ρ_c is the critical density of the

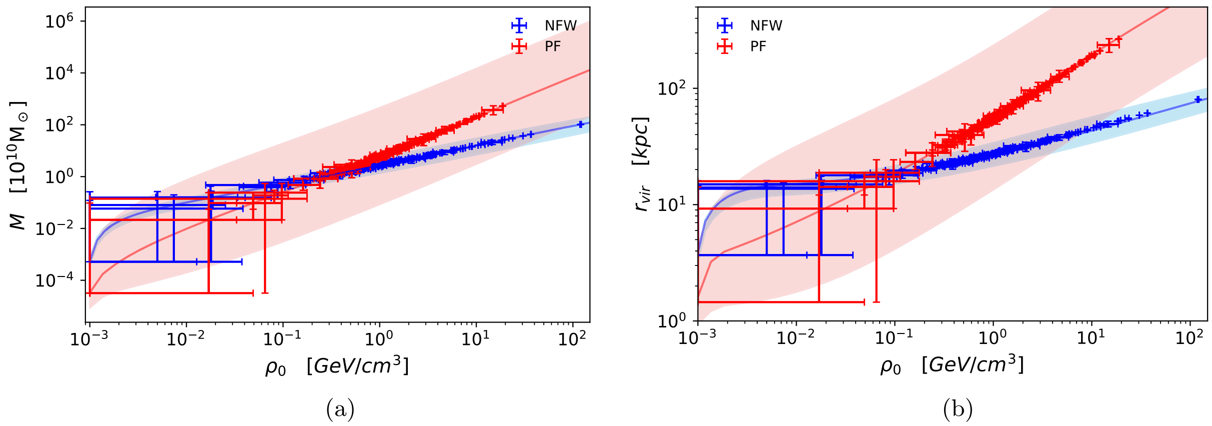

FIG. 12. Relations between the central density ρ_0 and the total mass (left) and virial radius (right) of the dark matter halos, for the perfect-fluid (red) and the NFW profile (blue) cases. Shaded regions represent the 68% confidence level for the values fermion mass and self-interacting parameter obtained from fitting the rotation curves of the LSB galaxies, the solid line represents the minimum. Error bars indicate the range of ρ_0 values for each galaxy at the 68% level and their corresponding total masses (left) or virial radii (right).

universe. There are interesting results that can be extracted from Fig. 11:

(1) The scaling relation found in [70,71] has been confirmed for both of our core-halo models. Most of the galaxies that we have analyzed have a central surface density μ_0 that falls within the range parametrized by Eq. (30). This result is relevant, as it is obtained after modifying the model for the dark matter pressure and applying it to two halo models as those considered in [70,71]. This suggests that the relation Eq. (30) might be a true scaling relation that all models for dark matter should satisfy.

(2) The lower panel indicates that although the constant central density surface density might be true, this relation does not imply a universal halo mass. Furthermore, as shown by Eqs. (31) and (32), the total mass of the dark matter core halo is a power law of the central density surface density μ_0. Combining rotation curve analysis with other observables, the gravitational lensing of the halo [72] for instance, could be used to distinguish between the perfect fluid or the NFW halo models, because they predict different halo masses.

In our case, the remaining 179 galaxies that we have fitted by varying only ρ_0 belong to a family of core halos. This fact is illustrated in Fig. 12. The left panel shows the typical plot M versus ρ_0 for the two halo models while the right panel shows the virial radius of the core-halo system r_{vir} vs ρ_0.

All galaxies can be seen as a particular realization of a self-gravitating object that is a solution of the TOV system with an EoS given by Eq. (5). Shaded regions represent the 68% confidence level for the values fermion mass and self-interacting parameter obtained from fitting the rotation curves of the LSB galaxies, the solid line represents the minimum. Error bars indicate the range of ρ_0 values for each galaxy at the 68%. There are important differences that depend on the halo model under consideration. The NFW halos are smaller and less massive than the perfect fluid ones, this is expected due to the fact that the density profile behaves as $\rho \sim r^{-2}$ for an isothermal gas sphere and as $\rho \sim r^{-3}$ for the NFW density profile.

A cosmological model with an equation of state as given by Eq. (5) lies beyond the analysis presented here. To our knowledge, the research beyond the pressureless hypothesis for dark matter is just starting. Current cosmological bounds for a barotropic equation of state are consistent with a pressure less dark matter EoS, although significant room for $p \neq 0$ is allowed [15–19]. At galactic scales, dark matter pressure could be required to understand some of the observation and alleviate tensions with the current CDM paradigm [20–23]. This work naturally extends the analysis for a fermionic dark matter particle that in the degenerate limit satisfies a polytropic effective EoS [26–29,53,54]. We found that if the self-interaction parameter y is zero, it is unlike that a single fermion can explain the diversity of halos. On the other hand, a single fermion with a significant contribution of self-interaction can explain a diversity of galaxies.

Note that the effective pressures obtained for the center of all the galaxies analyzed in this work fall below the cosmological limit for a barotropic equation of state for a halo modeled as a perfect fluid and just in the limit of testability for the NFW halos. This is illustrated in Fig. 14 where we have overlapped the limits obtained in [19] against the pressure obtained for the EoS (5) with the values for m_f and y as expressed in Eqs. (17) and (18). Furthermore, the data points correspond to the value of the pressure for the central density that explains the data for each of the 185 galaxies analyzed here. In can be inferred from Fig. 14 that galactic analysis could be more sensible to the pressureless hypothesis for dark matter.

To calculate the self-interacting cross section in a mean field theory with a Lagrangian given by $\mathcal{L}_{\mathrm{int}} = g\bar{\chi}\gamma_\mu\chi\mathbf{V}^\mu$, as shown in [73], the cross section is written as

$$\sigma = \frac{1}{4\pi}\frac{y^4}{m_f^2}\left[\frac{1}{1+r} - \frac{\ln(1+r)}{r(2+r)}\right], \tag{33}$$

where r is the defined as

$$r = \left(\frac{\beta_{\mathrm{rel}} m_f}{m_I}\right)^2 \tag{34}$$

and β_{rel} is the relative velocity between particles in the nonrelativistic limit. In our model the self-interacting parameter y includes in its definition both the coupling constant g and the mass of the particle that mediates the interaction, $y = gm_f/m_I$, as a result the cross-section cannot be uniquely determined from m_f and y alone. Nevertheless, rewriting the expression in terms of the coupling constant g

$$\sigma = \frac{1}{4\pi}\frac{y^4}{m_f^2}g^2\left[\frac{1}{g^2+y^2\beta_{\mathrm{rel}}^2} - \frac{g^2(\ln(g^2+y^2\beta_{\mathrm{rel}}^2) - \ln g^2)}{y^2\beta_{\mathrm{rel}}^2(2g^2+y^2\beta_{\mathrm{rel}}^2)}\right], \tag{35}$$

we can estimate what values of the coupling constant and the mediator mass would be consistent with the constraints of the bullet cluster [74]. With $\sigma/m < 1\ \mathrm{cm}^2/\mathrm{g}$ and $v_{\mathrm{rel}} \sim 3\times10^3$ km/s in galaxy clusters [75], corresponding to $\beta_{\mathrm{rel}} \sim 10^{-2}$, our results imply that, to be consistent with the Bullet Cluster constraints, the coupling constant should be $g \sim \mathcal{O}(10^{-13})$ for the NFW profile and $g \sim \mathcal{O}(10^{-14})$ for the perfect-fluid case, which would entail a mediator with a mass of $m_H \sim \mathcal{O}(10^{-13}\ \mathrm{eV})$ and $m_H \sim \mathcal{O}(10^{-15}\ \mathrm{eV})$, respectively.

It is important to point out that the self-interacting regime is confined to the degenerate core of our model, with radii below 2 kpc or 20 kpc depending on the halo type as seen in Fig. 13. Outside this region the model is described by a perfect fluid or NFW profile, which, as it dilutes, becomes an effectively pressureless EoS at the outskirts of the halo, equivalent to CDM.

As a consequence, a direct comparison to constraints obtained through simulations at cluster scales is not straightforward. Because of the size of the degenerate cores, it is not clear if the simulations would be sensitive to the degenerate region of the halo.

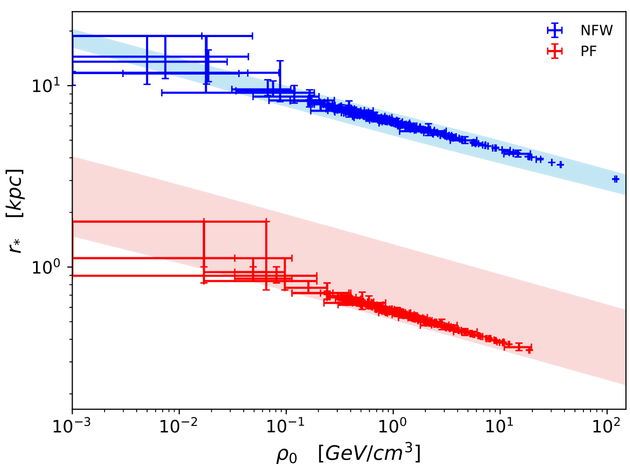

FIG. 13. Relation between the central density ρ_0 and transition radius r_* between the degenerate and halo regions of the dark matter halos, for the perfect-fluid (red) and the NFW profile (blue) cases. Shaded regions represent the 68% confidence level for the values fermion mass and self-interacting parameter obtained from fitting the rotation curves of the LSB galaxies. Error bars indicate the range of ρ_0 values for each galaxy at the 68% level and their corresponding degenerate core radii.

IX. CONCLUSIONS

Within certain conditions the quantum nature of the particle that conforms the dark matter must be taken into account, and the pressureless CDM paradigm must be challenged. For the case of a gas of fermionic particles this means becoming degenerate below a certain temperature. In the simplest model, this degenerate core depends on three parameters: the fermion mass, the central density of the system, and if the particle has self-interactions and its strength. Of these parameters, the two relevant ones to describe the particle that would make up dark matter are the fermion mass and the self-interaction parameter, since these must be universal and fundamental, while the central density is a parameter that changes from system to system.

Outside of this region of degeneracy the system must have a halo, we chose a perfect fluidlike halo, and a NFW type halo. Using six LSB galaxies we show that the inclusion of self-interactions yields better results when fitting the rotational curves. If the fermion has a perfect fluid halo, the mass must fall within the range of $155.10\ \mathrm{eV} < m_f < 313.26\ \mathrm{eV}$ and $1465.31 < y < 6002.04$ for the self-interaction parameter. If the halo is of the NFW type, then the values are $42.31\ \mathrm{eV} < m_f < 49.23\ \mathrm{eV}$ and $71.43 < y < 132.65$.

Fixing the fermion mass and self interacting parameter to the values that minimize the combined χ^2 of the LSB galaxies, there remains only one free parameter, the central density, a value that depends on the system studied. We tested the m_f and y parameters in two different cases: the Milky Way rotational curve and the SPARC dataset. The Milky Way's rotation curve can be decomposed into four components apart from the dark matter halo—the inner bulge, the main bulge, the disk, and the black hole. Of these baryonic components, all but the black hole are described by an exponential sphere model. Performing the central density fitting for the Milky Way, the best fit for the NFW halo case is $\chi^2/\mathrm{d.o.f.} = 0.94$, while it is $\chi^2/\mathrm{d.o.f.} = 0.79$ for the perfect fluid. The second case to test the core-halo model with a self-interacting degenerate fermion core was the SPARC dataset. This dataset includes 175 spiral and irregular galaxies and it includes the baryonic contributions of the gas, disk, and bulge of each galaxy. If the outer halo is of the perfect fluid type, the median $\chi^2/\mathrm{d.o.f.}$ is 2.85; for the NFW case, it is 6.09. Overall the case with a perfect fluid halo provided better fits for the LSB galaxies, the Milky Way, and SPARC dataset. By fixing m_f and y, there is only one free parameter, the central density ρ_0. This values are reported in Tables II, III, IV, and VIII. The matching condition of the degenerate fermion core and the halo determines ρ_s and r_s once ρ_0 is fitted by data. Since $\rho_s < \rho_0$, we can see that ρ_s is in reasonable agreement with the previous fit that used NFW profiles only for the dark matter halo [76].

The halos found in the analysis have certain structural properties that are interesting, such as the total mass of the halo having an exponential dependency to the central surface density, instead of the nearly constant value reported.

Our core-halo model predicts a core made of degenerate fermions. This condition of degeneracy is system dependent. Outside the degenerate core it becomes dilute and with negligible pressure at cosmological scales, behaving as a pressureless fluid at large scales. Furthermore, as it can be noted from Fig. 14, the central pressure where the fermions are degenerated is much smaller that the current limit for the pressure for dark matter obtained from PLANCK data [19] by assuming a barotropic equation of state for dark matter. Because of this we expect the model to reproduce the standard CDM results at large scales.

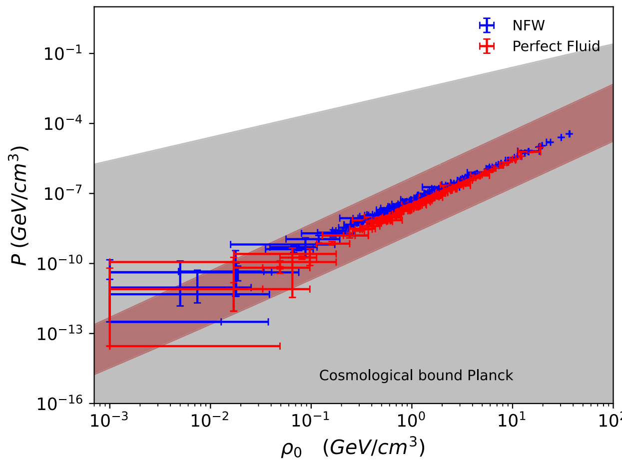

FIG. 14. Shaded gray region represents the current cosmological bound for a barotropic EoS for dark matter [19] and it is compared for the pressure obtained for the EoS given by Eq. (5) with m_f and y given by Eq. (17) for the NFW halo and Eq. (18) for the perfect fluid halo (brown shaded region). Data points correspond to the pressure at the center of each galaxy taken from Table VIII.

A proper cosmological simulation would require an analysis to calculate if these conditions are met at any moment in the evolution of the universe, which clearly is far beyond the scope of this work.

DATA AVAILABILITY

The data that support the findings of this article that are publicly available are included in the references. The data are available from the authors upon reasonable request.

APPENDIX: RESULTS FROM FITS TO SPARC DATASET

TABLE VIII. Summary of the fits for the SPARC catalog. The first column refers to the name of the galaxy. The two cases for the halo model are reported: the NFW halo and the perfect fluid halo. For each case we report: the first column is the best fit value for the central density ρ_0 in units of $\mathrm{GeV/cm^3}$ obtained form the fit as explained in Sec. VII. The second column shows the minimum value of the χ^2 function and the third column the goodness of the fit expressed with the value of the minimum of the χ^2 function divided by the degree of freedom. For completeness, some properties of each galaxy under analysis are reported as: Q the quality flag: 1 = High, 2= Medium, 3= Low. The Hubble type is obtained from [51,52] or NED and finally the number of data points N_{data}.

	NFW halo			Perfect fluid halo					
Galaxy	ρ_0 (GeV/cm^3)	χ^2	χ^2/d.o.f.	ρ_0 (GeV/cm^3)	χ^2	χ^2/d.o.f.	Q	Hubble type	N_{data}
CamB	0.075	32.268	4.034	0.081	33.266	4.158	2	Im	9
D512-2	0.386	11.618	3.873	0.497	6.625	2.208	2	Im	4
D564-8	0.192	9.990	1.998	0.241	4.942	0.988	2	Im	6
D631-7	0.300	10.246	0.683	0.481	34.920	2.328	1	Im	16
DDO064	0.915	11.258	0.866	1.042	7.938	0.611	1	Im	14
DDO154	0.332	1272.398	115.673	0.497	296.096	26.918	2	Im	12

(Table continued)

TABLE VIII. *(Continued)*

	NFW halo			Perfect fluid halo					
Galaxy	ρ_0 (GeV/cm^3)	χ^2	χ^2/d.o.f.	ρ_0 (GeV/cm^3)	χ^2	χ^2/d.o.f.	Q	Hubble type	N_{data}
DDO161	0.248	276.003	9.200	0.497	219.345	7.312	1	Im	31
DDO168	0.610	55.513	6.168	0.786	34.772	3.864	2	Im	10
DDO170	0.233	50.609	7.230	0.465	13.737	1.962	2	Im	8
ESO079-G014	3.249	601.878	42.991	3.187	194.939	13.924	1	Sbc	15
ESO116-G012	1.135	34.247	2.446	1.714	12.915	0.923	1	Sd	15
ESO444-G084	1.052	131.856	21.976	1.346	77.474	12.912	2	Im	7
ESO563-G021	6.280	2989.194	103.076	7.815	1281.477	44.189	1	Sbc	30
F561-1	0.067	5.805	1.161	0.161	2.617	0.523	3	Sm	6
F563-1	1.500	18.871	1.179	1.730	7.813	0.488	1	Sm	17
F563-V1	0.018	2.960	0.592	0.049	1.441	0.288	3	Im	6
F563-V2	1.814	8.381	0.931	2.403	5.454	0.606	1	Im	10
F565-V2	0.530	0.519	0.086	0.914	1.394	0.232	2	Im	7
F567-2	0.172	3.000	0.750	0.337	0.969	0.242	3	Sm	5
F568-1	1.932	1.895	0.172	2.467	0.620	0.056	1	Sc	12
F568-3	0.737	28.939	1.702	1.026	44.656	2.627	1	Sd	18
F568-V1	1.598	8.052	0.575	2.227	3.646	0.260	1	Sd	15
F571-8	1.481	321.556	26.796	2.147	257.761	21.480	1	Sc	13
F571-V1	0.530	4.225	0.704	0.882	1.902	0.317	2	Sd	7
F574-1	0.892	13.675	1.052	1.330	1.793	0.138	1	Sd	14
F574-2	0.005	0.294	0.074	0.017	0.354	0.088	3	Sm	5
F579-V1	1.538	38.637	2.972	1.938	31.811	2.447	1	Sc	14
F583-1	0.580	9.013	0.376	0.898	6.757	0.282	1	Sm	25
F583-4	0.354	15.247	1.386	0.641	8.713	0.792	1	Sc	12
IC2574	0.163	172.003	5.212	0.321	494.733	14.992	2	Sm	34
IC4202	3.332	1793.212	57.846	4.196	1272.909	41.062	1	Sbc	32
KK98-251	0.278	10.341	0.739	0.337	4.582	0.327	2	Im	15
NGC0024	1.481	342.594	12.235	1.874	273.310	9.761	1	Sc	29
NGC0055	0.372	42.817	2.141	0.657	78.886	3.944	2	Sm	21
NGC0100	0.625	6.080	0.304	0.994	4.257	0.213	1	Scd	21
NGC0247	0.756	468.670	18.747	1.122	198.396	7.936	2	Sd	26
NGC0289	6.863	760.733	28.175	3.876	136.736	5.064	2	Sbc	28
NGC0300	0.859	55.081	2.295	1.266	17.196	0.717	2	Sd	25
NGC0801	9.070	617.703	51.475	4.612	137.948	11.496	1	Sc	13
NGC0891	2.250	830.057	48.827	2.691	530.421	31.201	1	Sb	18

TABLE IX. SPARC fits comparison (part 2 of 5).

	NFW halo			Perfect fluid halo					
Galaxy	ρ_0 (GeV/cm^3)	χ^2	χ^2/d.o.f.	ρ_0 (GeV/cm^3)	χ^2	χ^2/d.o.f.	Q	Hubble type	N_{data}
NGC1003	1.288	2708.988	77.400	1.490	796.191	22.748	1	Scd	36
NGC1090	4.349	849.573	36.938	2.931	137.763	5.990	1	Sbc	24
NGC1705	1.224	212.471	16.344	1.682	146.950	11.304	3	BCD	14
NGC2366	0.340	157.553	6.302	0.513	55.728	2.229	3	Im	26
NGC2403	1.500	8359.532	116.105	2.067	2061.135	28.627	1	Scd	73
NGC2683	3.418	55.956	5.596	3.348	6.141	0.614	2	Sb	11
NGC2841	30.421	7144.075	145.797	12.074	299.863	6.120	1	Sb	50
NGC2903	3.128	2398.145	72.671	3.315	756.719	22.931	1	Sbc	34
NGC2915	0.766	67.022	2.311	1.218	42.857	1.478	2	BCD	30
NGC2955	1.372	258.424	11.236	2.259	190.191	8.269	1	Sb	24
NGC2976	2.367	11.541	0.444	2.515	9.388	0.361	2	Sc	27
NGC2998	13.266	514.322	42.860	5.333	93.259	7.772	1	Sc	13
NGC3109	0.473	52.548	2.190	0.738	6.499	0.271	1	Sm	25
NGC3198	1.957	7290.156	173.575	2.547	1214.434	28.915	1	Sc	43
NGC3521	3.049	123.506	3.088	3.700	47.638	1.191	1	Sbc	41
NGC3726	1.224	163.382	14.853	1.698	84.163	7.651	2	Sc	12
NGC3741	0.300	153.944	7.697	0.497	54.644	2.732	1	Im	21
NGC3769	1.179	62.454	5.678	1.586	18.779	1.707	2	Sb	12
NGC3877	1.272	51.097	4.258	1.794	53.192	4.433	2	Sc	13
NGC3893	2.721	30.301	3.367	3.155	6.360	0.707	1	Sc	10
NGC3917	1.462	71.463	4.466	1.986	24.507	1.532	1	Scd	17
NGC3949	1.079	2.916	0.486	1.586	3.527	0.588	2	Sbc	7
NGC3953	3.088	11.297	1.614	3.460	1.275	0.182	1	Sbc	8
NGC3972	1.304	17.584	1.954	1.954	7.421	0.825	1	Sbc	10
NGC3992	18.211	254.943	31.868	7.815	17.645	2.206	1	Sbc	9
NGC4010	0.975	27.491	2.499	1.506	30.611	2.783	2	Sd	12
NGC4013	3.596	1184.242	33.835	3.091	341.036	9.744	2	Sb	36
NGC4051	0.837	2.376	0.396	1.266	3.410	0.568	2	Sbc	7
NGC4068	0.456	0.964	0.193	0.513	1.137	0.227	2	Im	6
NGC4085	0.737	23.954	3.992	1.138	27.425	4.571	2	Sc	7
NGC4088	0.610	84.855	7.714	1.074	62.769	5.706	1	Sbc	12
NGC4100	3.550	135.071	5.873	3.460	14.742	0.641	1	Sbc	24
NGC4138	2.427	1.805	0.301	2.787	5.116	0.853	2	S0	7
NGC4157	2.619	174.583	10.911	2.611	70.499	4.406	1	Sb	17
NGC4183	1.209	57.222	2.601	1.490	10.818	0.492	1	Scd	23
NGC4214	1.256	90.956	6.997	1.746	65.685	5.053	2	Im	14
NGC4217	0.450	730.019	40.557	0.978	720.999	40.055	1	Sb	19
NGC4389	0.001	83.915	16.783	0.001	83.899	16.780	3	Sbc	6
NGC4559	1.135	194.364	6.270	1.458	58.549	1.889	1	Scd	32
NGC5005	2.138	14.179	0.834	2.851	13.325	0.784	1	Sbc	18

TABLE X. SPARC fits comparison (part 3 of 5).

	NFW halo			Perfect fluid halo					
Galaxy	ρ_0 (GeV/cm^3)	χ^2	χ^2/d.o.f.	ρ_0 (GeV/cm^3)	χ^2	χ^2/dof	Q	Hubble type	N_{data}
NGC5033	10.427	1884.089	89.719	5.381	260.485	12.404	1	Sc	22
NGC5055	1.558	34157.836	1265.105	2.435	14853.161	550.117	1	Sbc	28
NGC5371	3.642	521.579	28.977	2.979	171.696	9.539	1	Sbc	19
NGC5585	0.701	125.189	5.443	1.074	126.406	5.496	1	Sd	24
NGC5907	13.266	1999.066	111.059	5.669	210.600	11.700	1	Sc	19
NGC5985	19.650	2420.273	75.634	10.681	86.643	2.708	1	Sb	33
NGC6015	2.619	2017.190	46.911	3.107	855.543	19.896	2	Scd	44
NGC6195	1.372	457.251	20.784	2.243	273.580	12.435	1	Sb	23
NGC6503	1.519	1356.585	45.219	1.762	121.255	4.042	1	Scd	31
NGC6674	120.202	2314.713	144.670	9.032	193.781	13.842	1	Sb	15
NGC6674	36.553	2052.109	146.579	9.032	193.781	13.842	1	Sb	15
NGC6789	14.681	0.197	0.066	15.004	0.350	0.117	2	BCD	4
NGC6946	1.408	535.461	9.394	1.970	276.056	4.843	1	Scd	58
NGC7331	5.820	3218.030	91.944	4.228	1321.483	37.757	1	Sb	36
NGC7793	1.079	133.979	2.977	1.554	94.918	2.109	1	Sd	46
NGC7814	5.675	433.148	25.479	4.869	65.531	3.855	1	Sab	18
PGC51017	0.007	8.776	1.755	0.017	8.828	1.766	3	BCD	6
UGC00128	3.462	8898.012	423.715	2.387	1308.150	62.293	1	Sdm	22
UGC00191	0.504	368.155	46.019	0.914	215.314	26.914	1	Sm	9
UGC00634	1.256	181.658	60.553	1.506	45.429	15.143	2	Sm	4
UGC00731	0.450	129.682	11.789	0.786	54.320	4.938	1	Im	12
UGC00891	0.308	8.025	2.006	0.577	16.209	4.052	2	Sm	5
UGC01230	1.372	13.972	1.397	1.618	1.878	0.188	1	Sm	11
UGC01281	0.492	22.302	0.929	0.690	6.394	0.266	1	Sdm	25
UGC02023	0.386	0.378	0.094	0.513	0.890	0.223	2	Im	5
UGC02259	0.870	321.838	45.977	1.362	173.835	24.834	2	Sdm	8
UGC02455	0.001	188.327	26.904	0.001	188.311	26.902	3	Im	8
UGC02487	25.000	18876.248	1179.766	18.751	132.382	8.274	1	S0	17
UGC02885	23.607	952.406	52.911	10.393	182.705	10.150	1	Sc	19
UGC02916	1.000	2381.415	56.700	1.650	2295.946	54.665	2	Sab	43
UGC02953	14.496	48482.022	425.281	8.792	4442.007	38.965	2	Sab	115
UGC03205	8.956	2446.804	52.060	5.381	287.954	6.127	1	Sab	48
UGC03546	4.240	941.351	32.460	3.428	273.325	9.425	1	Sa	30
UGC03580	1.092	4181.832	90.909	1.458	2630.997	57.196	2	Sa	47
UGC04278	0.650	18.116	0.755	0.994	30.023	1.251	1	Sd	25
UGC04305	0.019	57.956	2.760	0.049	53.090	2.528	3	Im	22
UGC04325	1.304	265.886	37.984	1.906	173.012	24.716	1	Sm	8
UGC04483	0.848	30.943	4.420	0.914	25.222	3.603	2	Im	8
UGC04499	0.417	31.700	3.963	0.738	6.770	0.846	1	Sdm	9
UGC05005	0.467	44.807	4.481	0.850	23.582	2.358	1	Im	11

TABLE XI. SPARC fits comparison (part 4 of 5).

	NFW halo			Perfect fluid halo					
Galaxy	ρ_0 (GeV/cm^3)	χ^2	χ^2/d.o.f.	ρ_0 (GeV/cm^3)	χ^2	χ^2/d.o.f.	Q	Hubble type	N_{data}
UGC05253	4.460	6990.842	97.095	4.677	1953.278	27.129	2	Sab	73
UGC05414	0.517	9.155	1.831	0.706	2.381	0.476	1	Im	6
UGC05716	0.456	358.821	32.620	0.754	89.173	8.107	2	Sm	12
UGC05721	1.012	426.984	19.408	1.554	303.699	13.804	1	Sd	23
UGC05750	0.261	4.931	0.493	0.481	7.401	0.740	1	Sdm	11
UGC05764	1.321	1647.441	183.049	1.554	1083.301	120.367	2	Im	10
UGC05829	0.328	10.610	1.061	0.545	2.957	0.296	2	Im	11
UGC05918	0.345	26.668	3.810	0.497	15.316	2.188	2	Im	8
UGC05986	1.408	56.508	4.036	2.067	21.344	1.525	2	Sm	15
UGC05999	0.658	28.378	7.095	1.026	19.645	4.911	2	Im	5
UGC06399	0.692	7.966	0.996	1.122	0.873	0.109	1	Sm	9
UGC06446	0.719	102.009	6.376	1.154	55.359	3.460	1	Sd	17
UGC06614	1.982	217.732	18.144	2.403	127.994	10.666	1	Sa	13
UGC06628	0.018	4.074	0.679	0.065	3.233	0.539	2	Sm	7
UGC06667	0.796	43.025	5.378	1.250	9.597	1.200	1	Scd	9
UGC06786	7.692	8929.987	202.954	6.374	901.169	20.481	1	S0	45
UGC06787	7.220	17358.013	247.972	6.230	4303.018	61.472	2	Sab	71
UGC06818	0.367	9.193	1.313	0.609	19.099	2.728	2	Sm	8
UGC06917	0.950	12.985	1.299	1.458	2.156	0.216	1	Sm	11
UGC06923	0.692	5.077	1.015	1.026	2.063	0.413	2	Im	6
UGC06930	0.950	12.594	1.399	1.362	1.604	0.178	1	Sd	10
UGC06973	0.382	619.401	77.425	0.593	638.980	79.872	3	Sab	9
UGC06983	1.106	29.848	1.865	1.618	10.021	0.626	1	Scd	17
UGC07089	0.315	3.026	0.275	0.561	5.810	0.528	2	Sdm	12
UGC07125	0.190	11.600	0.967	0.385	7.611	0.634	1	Sm	13
UGC07151	0.747	162.726	16.273	1.090	92.254	9.225	1	Scd	11
UGC07232	4.692	0.391	0.130	4.677	0.321	0.107	2	Im	4
UGC07261	0.587	29.183	4.864	0.978	17.585	2.931	2	Sdm	7
UGC07323	0.565	4.591	0.510	0.866	3.180	0.353	1	Sdm	10
UGC07399	1.908	300.018	33.335	2.579	174.982	19.442	1	Sdm	10
UGC07524	0.473	52.923	1.764	0.802	10.225	0.341	1	Sm	31
UGC07559	0.328	2.784	0.464	0.385	1.707	0.285	2	Im	7
UGC07577	0.088	0.535	0.067	0.097	0.642	0.080	2	Im	9
UGC07603	0.903	120.260	10.933	1.218	72.781	6.616	1	Sd	12
UGC07608	0.719	5.802	0.829	1.010	1.756	0.251	1	Im	8
UGC07690	0.572	48.410	8.068	0.818	38.159	6.360	2	Im	7
UGC07866	0.428	5.380	0.897	0.481	4.307	0.718	2	Im	7
UGC08286	0.786	569.823	35.614	1.250	312.461	19.529	1	Scd	17
UGC08490	0.683	405.417	13.980	1.106	282.014	9.725	1	Sm	30
UGC08550	0.485	246.394	24.639	0.754	148.222	14.822	1	Sd	11

TABLE XII. SPARC fits comparison (part 5 of 5).

	NFW halo			Perfect fluid halo					
Galaxy	ρ_0 (GeV/cm^3)	χ^2	χ^2/d.o.f.	ρ_0 (GeV/cm^3)	χ^2	χ^2/d.o.f.	Q	Hubble type	N_{data}
UGC08699	2.973	522.994	13.075	3.460	135.662	3.392	2	Sab	41
UGC08837	0.227	4.921	0.703	0.305	10.215	1.459	2	Im	8
UGC09037	0.625	415.126	19.768	1.154	323.120	15.387	2	Scd	22
UGC09133	18.678	43435.103	648.285	7.863	3593.666	53.637	1	Sab	68
UGC09992	0.165	6.673	1.668	0.241	5.310	1.328	2	Im	5
UGC10310	0.473	24.072	4.012	0.818	9.968	1.661	1	Sm	7
UGC11455	3.880	1507.863	43.082	4.564	694.647	19.847	1	Scd	36
UGC11557	0.119	12.776	1.161	0.241	15.733	1.430	2	Sdm	12
UGC11820	0.450	329.485	36.609	0.754	145.212	16.135	1	Sm	10
UGC11914	5.603	1313.744	20.527	6.726	1024.021	16.000	1	Sab	65
UGC12506	14.314	345.037	11.501	7.751	25.611	0.854	2	Scd	31
UGC12632	0.406	50.828	3.631	0.722	13.522	0.966	1	Sm	15
UGC12732	0.666	84.249	5.617	1.026	24.092	1.606	1	Sm	16
UGCA281	1.860	29.389	4.898	2.003	24.802	4.134	3	BCD	7
UGCA442	0.292	101.638	14.520	0.561	25.083	3.583	1	Sm	8
UGCA444	0.595	42.508	1.215	0.657	34.084	0.974	2	Im	36

[1] N. Aghanim *et al.* (Planck Collaboration), Astron. Astrophys. **641**, A6 (2020); **652**, C4(E) (2021).
[2] J. F. Navarro, C. S. Frenk, and S. D. M. White, Astrophys. J. **490**, 493 (1997).
[3] J. S. Bullock and M. Boylan-Kolchin, Annu. Rev. Astron. Astrophys. **55**, 343 (2017).
[4] A. A. Klypin, A. V. Kravtsov, O. Valenzuela, and F. Prada, Astrophys. J. **522**, 82 (1999).
[5] M. Boylan-Kolchin, J. S. Bullock, and M. Kaplinghat, Mon. Not. R. Astron. Soc. **415**, L40 (2011).
[6] M. S. Pawlowski, Mod. Phys. Lett. A **33**, 1830004 (2018).
[7] S. McGaugh, Astron. J. **143**, 40 (2012).
[8] J. T. Kleyna, M. I. Wilkinson, G. Gilmore, and N. W. Evans, Astrophys. J. Lett. **588**, L21 (2003); **589**, L59(E) (2003).
[9] J. D. Simon and M. Geha, Astrophys. J. **670**, 331 (2007).
[10] A. El-Zant, I. Shlosman, and Y. Hoffman, Astrophys. J. **560**, 636 (2001).
[11] J. F. Navarro, V. R. Eke, and C. S. Frenk, Mon. Not. R. Astron. Soc. **283**, L72 (1996).
[12] A. Zolotov, A. M. Brooks, B. Willman, F. Governato, A. Pontzen, C. Christensen, A. Dekel, T. Quinn, S. Shen, and J. Wadsley, Astrophys. J. **761**, 71 (2012).
[13] A. M. Brooks and A. Zolotov, Astrophys. J. **786**, 87 (2014).
[14] M. S. TurnerarXiv:2201.04741.
[15] C. M. Muller, Phys. Rev. D **71**, 047302 (2005).
[16] E. Calabrese, M. Migliaccio, L. Pagano, G. De Troia, A. Melchiorri, and P. Natoli, Phys. Rev. D **80**, 063539 (2009).
[17] S. Kumar and L. Xu, Phys. Lett. B **737**, 244 (2014).
[18] C. Armendariz-Picon and J. T. Neelakanta, J. Cosmol. Astropart. Phys. 03 (2014) 049.
[19] L. Xu and Y. Chang, Phys. Rev. D **88**, 127301 (2013).
[20] A. L. Serra and M. J. d. L. D. Romero, Mon. Not. R. Astron. Soc. **415**, L74 (2011).
[21] J. Barranco, A. Bernal, and D. Nunez, Mon. Not. R. Astron. Soc. **449**, 403 (2015).
[22] A. Aceña, J. Barranco, A. Bernal, E. López, and M. Llerena, Astrophys. J. **970**, 186 (2024).
[23] K. Boshkayev, T. Konysbayev, E. Kurmanov, O. Luongo, D. Malafarina, K. Mutalipova, and G. Zhumakhanova, Mon. Not. R. Astron. Soc. **508**, 1543 (2021).
[24] W. Hu, R. Barkana, and A. Gruzinov, Phys. Rev. Lett. **85**, 8 (2000).
[25] D. Koester and G. Chanmugam, Rep. Prog. Phys. **53**, 837 (1990).
[26] V. Domcke and A. Urbano, J. Cosmol. Astropart. Phys. 01 (2015) 002.
[27] L. Randall, J. Scholtz, and J. Unwin, Mon. Not. R. Astron. Soc. **467**, 1515 (2017).
[28] H. J. de Vega and N. G. Sanchez, arXiv:1304.0759.
[29] C. Destri, H. J. D. Vega, and N. G. Sanchez, New Astron. **22**, 39 (2013).
[30] P.-H. Chavanis, Phys. Rev. E **65**, 056123 (2002).
[31] P.-H. Chavanis, M. Lemou, and F. Méhats, Phys. Rev. D **91**, 063531 (2015).
[32] C. R. Argüelles, E. A. Becerra-Vergara, J. A. Rueda, and R. Ruffini, Universe **9**, 197 (2023).

[33] P.-H. Chavanis, Phys. Rev. D **106**, 043538 (2022).
[34] E. D. Carlson, M. E. Machacek, and L. J. Hall, Astrophys. J. **398**, 43 (1992).
[35] A. A. de Laix, R. J. Scherrer, and R. K. Schaefer, Astrophys. J. **452**, 495 (1995).
[36] C. Firmani, E. D'Onghia, V. Avila-Reese, G. Chincarini, and X. Hernandez, Mon. Not. R. Astron. Soc. **315**, L29 (2000).
[37] D. N. Spergel and P. J. Steinhardt, Phys. Rev. Lett. **84**, 3760 (2000).
[38] M. Vogelsberger and J. Zavala, Mon. Not. R. Astron. Soc. **430**, 1722 (2013).
[39] J. Sánchez Almeida and I. Trujillo, Mon. Not. R. Astron. Soc. **504**, 2832 (2021).
[40] A. Kamada, M. Kaplinghat, A. B. Pace, and H.-B. Yu, Phys. Rev. Lett. **119**, 111102 (2017).
[41] S. Chandrasekhar, *An Introduction to the Study of the Stellar Structure* (University of Chicago Press, Chicago, 1939).
[42] B. D. Serot and J. D. Walecka, *Relativistic Nuclear Many-Body Theory* (Springer US, Boston, MA, 1992), pp. 49–92.
[43] H. Shen, H. Toki, K. Oyamatsu, and K. Sumiyoshi, Nucl. Phys. **A637**, 435 (1998).
[44] J. Ren, X.-Q. Li, and H. Shen, Commun. Theor. Phys. **49**, 212 (2008).
[45] G. Narain, J. Schaffner-Bielich, and I. N. Mishustin, Phys. Rev. D **74**, 063003 (2006).
[46] R. Stiele, T. Boeckel, and J. Schaffner-Bielich, Phys. Rev. D **81**, 123513 (2010).
[47] B. W. Carroll and D. A. Ostlie, *An Introduction to Modern Astrophysics* (Addison-Wesley, San Francisco, CA, 2007).
[48] W. J. G. de Blok and S. S. McGaugh, Mon. Not. R. Astron. Soc. **290**, 533 (1997).
[49] W. J. G. de Blok, S. S. McGaugh, and V. C. Rubin, Astron. J. **122**, 2396 (2001).
[50] S. S. McGaugh, V. C. Rubin, and W. J. G. de Blok, Astron. J. **122**, 2381 (2001).
[51] G. de Vaucouleurs, A. de Vaucouleurs, H. G. Corwin, Jr., R. J. Buta, G. Paturel, and P. Fouque, *Third Reference Catalogue of Bright Galaxies* (Springer, New York, 1991).
[52] J. M. Schombert, G. D. Bothun, S. E. Schneider, and S. S. McGaugh, Astron. J. **103**, 1107 (1992).
[53] C. Destri, H. J. D. Vega, and N. G. Sanchez, Astropart. Phys. **46**, 14 (2013).
[54] J. Barranco, A. Bernal, and D. Delepine, J. Phys. G **53**, 025002 (2026).
[55] Y. Sofue, M. Honma, and T. Omodaka, Publ. Astron. Soc. Jpn. **61**, 227 (2009).
[56] Y. Sofue, Publ. Astron. Soc. Jpn. **65**, 118 (2013).
[57] A. M. Ghez *et al.*, Astrophys. J. **689**, 1044 (2008).
[58] M. G. Walker, M. Mateo, E. W. Olszewski, J. Peñarrubia, N. W. Evans, and G. Gilmore, Astrophys. J. **704**, 1274 (2009).
[59] M. G. Walker, M. Mateo, E. W. Olszewski, O. Y. Gnedin, X. Wang, B. Sen, and M. Woodroofe, Astrophys. J. Lett. **667**, L53 (2007).
[60] M. Mateo, E. W. Olszewski, and M. G. Walker, Astrophys. J. **675**, 201 (2008).
[61] M. G. Walker, M. Mateo, and E. W. Olszewski, Astron. J. **137**, 3100 (2009).
[62] F. Lelli, S. S. McGaugh, and J. M. Schombert, Astron. J. **152**, 157 (2016).
[63] T. S. van Albada, J. N. Bahcall, K. Begeman, and R. Sancisi, Astrophys. J. **295**, 305 (1985).
[64] M. Eskew, D. Zaritsky, and S. Meidt, Astron. J. **143**, 139 (2012).
[65] S.-H. Oh, W. J. G. de Blok, F. Walter, E. Brinks, and R. C. Kennicutt, Astron. J. **136**, 2761 (2008).
[66] S. E. Meidt *et al.*, Astrophys. J. **788**, 144 (2014).
[67] J. Schombert, S. McGaugh, and F. Lelli, Mon. Not. R. Astron. Soc. **483**, 1496 (2018).
[68] J. Schombert and S. McGaugh, Pub. Astron. Soc. Aust. **31**, e036 (2014).
[69] S. S. McGaugh, F. Lelli, and J. M. Schombert, Phys. Rev. Lett. **117**, 201101 (2016).
[70] F. Donato, G. Gentile, P. Salucci, C. F. Martins, M. I. Wilkinson, G. Gilmore, E. K. Grebel, A. Koch, and R. Wyse, Mon. Not. R. Astron. Soc. **397**, 1169 (2009).
[71] G. Gentile, B. Famaey, H. Zhao, and P. Salucci, Nature (London) **461**, 627 (2009).
[72] D. Nunez, A. X. Gonzalez-Morales, J. L. Cervantes-Cota, and T. Matos, Phys. Rev. D **82**, 024025 (2010).
[73] S. Girmohanta and R. Shrock, Phys. Rev. D **106**, 063013 (2022).
[74] M. Markevitch, A. H. Gonzalez, D. Clowe, A. Vikhlinin, W. Forman, C. Jones, S. Murray, and W. Tucker, Astrophys. J. **606**, 819 (2004).
[75] S. Tulin and H.-B. Yu, Phys. Rep. **730**, 1 (2018).
[76] R. Jimenez, L. Verde, and S. P. Oh, Mon. Not. R. Astron. Soc. **339**, 243 (2003).